Detecting diverse types of cardiovascular brain pulses in Alzheimer's disease simultaneously with fNIRS and MREG

Bebelo Masena
Pro gradu thesis
Biomedical Physics
Research unit of Nano and Molecular systems
University of Oulu
2023

CONTENTS

1 ABSTRACT

One of the risk factors for Alzheimer's disease is hypertension. Hypertension alters the brain's blood vessel structure due to increased arterial pressure. Structural changes in the blood vessels are seen in the cardiovascular pulse, which is formed by blood velocity, blood flow rate, blood pressure, and infrequently blood flow. By simultaneously applying magnetic resonance encephalography (MREG) and functional near-infrared spectroscopy (fNIRS), this study discovered cardiovascular brain pulses from the blood flow within patients with Alzheimer's disease and healthy controls. This study detects specific parameters within diverse types of cardiovascular brain pulses. The results detected changes in parameters for diverse types of cardiovascular brain pulses in patients with Alzheimer's disease within MREG and fNIRS. In addition, the results present an alternative method for finding cardiovascular brain pulse from the blood flow, which might reflect the structural changes of a blood vessel in patients with Alzheimer's disease. In conclusion, diverse types of cardiovascular brain pulses represent an approximation of arterial, venous, and tissue pulses, which is beneficial for distinguishing the effect of venous and arterial hypertension in Alzheimer's disease. Furthermore, altered blood flow may potentially be associated with the impaired glymphatic system in Alzheimer's disease.

2 ABBREVIATIONS

AA	Alzheimer's Association
Aβ	Amyloid-β
AD	Alzheimer's disease
ApoE	Apolipoprotein E
AQ4	Aquaporin-4
BBB	Blood-brain barrier
BLL	Beer-Lamber law
BOLD	Blood oxygen level-dependent
CBP	Cardiovascular brain pulse
CNS	Cerebral nervous system
CSF	Cerebrospinal fluid
DSM-5	Diagnostic and Statistical Manual of Mental Disorders, Fifth Edition
FNIRS	Functional near-infrared spectroscopy
FMRI	Functional magnetic resonance imaging
FWHM	Full width with half-maximum
HbO	Oxyhemoglobin
HbR	Deoxyhemoglobin
HbT	Total hemoglobin
H_2O	Water
ISF	Interstitial fluid
MBLL	Modified Beer-Lambert law
MCI	Mild cognitive impairment
MMSE	Mini-mental state examination
MPRAGE	Magnetization-prepared and rapid gradient-echo
MREG	Magnetic resonance encephalography
MRI	Magnetic resonance imaging
NFT	Neurofibrillary tangle
NIA	The National Institute on Aging
NMR	Nuclear magnetic resonance
PA	Pulse amount
PA_1	The first pulse angle

PA_2	The second pulse angle
PD	Pulse duration
PFD	Pulse fall duration
PRD	Pulse rise duration
RF	Radio frequency

3 INTRODUCTION

AD is the most common neurodegenerative disease that increasingly burdens global health care. AD characteristically manifests as slow cerebral accumulation of amyloid-β plaques over decades, often accompanied by hyperphosphorylated tau tangles in degenerating neurons and periarteriolar structures [1]–[3]. Unfortunately, clinical trials with gamma-secretase enzyme inhibitors or antibodies against Aβ protein aggregates have failed to change disease progression [4], [5]. Growing recognition of Aβ accumulations is necessary but insufficient for AD pathology [6]. Hence, an ideal biomarker for diagnosing incipient AD would be minimally invasive and sensitive to the brain pathology occurring at an early disease stage.

The heart produces the cardiovascular pulse by contracting the chambers, moving the blood to arteries from the aorta, and returning the blood to the heart through veins. The propagation of the cardiovascular pulse can be described by blood velocity, blood flow rate, and blood pressure [7]. Multiple studies show that the progression of dementia connects to cerebrovascular disease, where elevated blood pressure [8]–[10] is associated with hypertension. Hypertension in mid-life is a well-established risk factor for AD [11]–[13]. Hypertension is also associated with a higher amyloid burden in the brain [14] and hippocampal atrophy [15] in the absence of clinical dementia. Increased arterial stiffness is suggested to be the primary mechanism conveying the detrimental effects of hypertension on the function and structure of the brain. Arterial stiffness is caused by increased pulsatility blood pressure. Reduced elasticity of vessel walls is generated from increased systolic blood pressure and decreased diastolic blood pressure [7], [16], [17]. Hence, long-lasting structural changes take place in the vessel wall and alter coronary perfusion [18], which are caused by hypertension [16], [19]. Tight control of blood pressure and nutritional and lifestyle changes, which minimize cardiovascular risk factors [20], can reduce or prevent conversion from MCI to AD

The glymphatic system is described as a waste clearance system of the brain [21]–[23]. The function of the glymphatic system begins when CSF is driven into the Virchow-Robin spaces by a combination of not only arterial pulsatility but recently also respiratory and slow vasomotion, which have been shown as drivers of CSF [21]–[23]. Then, CSF continues its flow into periarterial spaces and converts into the brain parenchyma as interstitial fluid via AQP4 water channels. Finally, CSF continues from the interstitial brain parenchyma to the perivenous space, where it drives into the CNS. The impaired glymphatic system is linked to AD [24], [25], narcolepsy [26], normal pressure hydrocephalus [25], [27], epilepsy [28], [29], and other neurodegenerative diseases [21], [30]. Due to AD pathology, depolarisation of AQ4 water channels and decreased cerebral blood flow impairs the glymphatic system.

Ultrafast 10 Hz whole-brain MREG, which reflects brain blood flow oxygenation and hydrodynamics, has enabled robust characterization of three human brain pulsation sources: the vasomotor, cardiac, and respiratory brain pulsations [23], [31]. However, no fMRI technique can

simultaneously differentiate sub-second pulsation dynamics between different blood compartments or the closely related hydrodynamics effects on the brain tissue. Therefore, a non-invasive method that could selectively quantify information on cardiovascular pulsation in each brain fluid compartment, could bring forth critical issues on the underlying pathophysiology in diseases like neurodegeneration.

FNIRS offers a non-invasive brain sensing technique that applies penetrating infrared light to capture reflective changes in tissue dynamics [32]–[34]. In addition, multiple studies have recently shown the capability of measuring brain water dynamics from the brain [32], [33]. Hence, this technology enables selective quantifying cerebral hydrodynamics in the human brain simultaneously in addition to more commonly used HbO and HbR metrics of brain hemodynamics.

AD patients and healthy controls were scanned simultaneously with fNIRS and MREG. MREG and fNIRS data were filtered at the cardiac frequency band to determine four CBP types from the CBP parameters. In this study, the diverse CBP types of parameters were altered in AD patients, hence providing insight regarding the changes in human brain water and compartments of hemodynamics. Furthermore, these results demonstrate that changes in CBP be indicative of structural alterations in brain blood vessels among AD patients. The results detected identical changes between FNIRS of the brain fluid compartment and MREG. Hence, comparing AD patients and healthy controls indicated that both imaging methods reflected the same underlying pathological phenomenon. In conclusion, measuring the CBP simultaneously with fNIRS and MREG might detect an impaired glymphatic system caused by AD. In contrast, an impaired glymphatic clearance system may be connected to impaired cerebral autoregulation.

4 BACKGROUND

4.1 AD

AD was discovered in 1907 when Alois Alzheimer detected several progressive and fatal neurological conditions. In addition, Alois Alzheimer also detected a new pathological entity called NFT. AD is a neurodegenerative disorder featuring gradually progressive cognitive, functional deficits, and behavioural changes caused by neuronal loss in the brain due to the increased accumulation of αβ and τ. AD's most common cognitive symptoms include deficits in short-term memory, executive and visuospatial dysfunction, and praxis. Risk factors for AD development are the presence of one or more apolipoprotein gene E4 alleles, age, low educational and occupational attainment, family history of AD, moderate or severe traumatic brain injuries, and cardiovascular risk factors. [35]

4.1.1 Clinical diagnostic

DSM-5 is a diagnostic standard for dementia based on primary and mild neurocognitive impairment. Symptoms of primary neurocognitive impairment require mild interference in activities of daily living due to cognitive decline, but it is not affected by other neurologic, medical, or psychiatric disorders. A patient with mild neurocognitive impairment can still live independently and perform complex daily activities despite the milder cognitive decline. The NIA and the AA have developed diagnostic criteria for the progress of AD, which are preclinical, prodromal, and overt dementia. The earliest symptoms of AD are apathy, anxiety, irritability, anosognosia, and depressive symptoms. Language disturbance can also be found in the early AD stage but is seen in the mild stage. Progression of decline in visuospatial skills occurs in the mild dementia stages. Later stages of dementia occur in sleep disturbance, disinhibition, and alterations in perception or thought. The NIA-AA criteria do not require memory impairment for determining dementia, like the DSM-5 criteria. However, the diagnosis of dementia by NIA-AA criteria is acquired by obtaining documentation of impairment in two cognitive domains or one cognitive and one behavioural, in addition to a considerable decline in activities of daily basis life. [35]

Biomarkers, such as CSF-Aβ, τ protein levels, and amyloid positron emission tomography support the clinical diagnosis of AD. CSF-Aβ and τ protein levels are measured from diagnostically challenging cases and early disease onset. For instance, the correlation between CSF-Aβ level and the amount of amyloid deposition in the cortex increases. Amyloid positron emission tomography imaging detects highly increased amyloid deposition in the brain and can potentially affect the procedure for diagnosing AD. The guidelines of a diagnostic evaluation of dementia from the American Academy of Neurology require a structural imaging scan, such as computational tomography imaging and MRI, in every patient that suffers an objective cognitive decline. MMSE is used for supporting clinical diagnosis in dementia by estimating the cognitive decline of patients,

where decreased MMSE score corresponds to the level of cognitive decline in various stages of dementia. [35], [36]

4.1.2 AD pathology

The primary pathology of AD is from tau hyperphosphorylation, neuronal toxicity and overproduction of Aβ deposits, and attenuated clearance of Aβ peptides. The pathologic features of AD are deprivation of synapses, brain atrophy, increased amyloid plaques, increased intraneuronal neurofibrillary tangles, and senile plaque. The cerebral blood vessels also suffer from the overproduction of Aβ deposits, called cerebral amyloid angiopathy [35]. The extracellular deposition of Aβ peptide and the intracellular aggregation of τ-protein in the pathology of AD causes most of the lesions in the brain. [37]

4.1.2.1 Aβ pathology

Aβ peptide is based on the amyloid protein precursor. Amyloid protein precursor is from cleaved amino acid of (Aβ) by β-secretase and a transmembrane protein based on γ-secretase, such as presenilin-1 and 2. In addition, γ-secretase contains a mixture of various Aβ isoforms, such as Aβ 39-42. The Aβ peptide can spontaneously and intracellularly oligomerize into Aβ-derived diffusible ligands with an aptitude for toxins. The accumulation of Aβ peptide occasionally begins in the vessel walls. It deposits around the basement membrane into the media and happens, for example, in lobar haemorrhages and small cortical. In the media, a double barrel and fibrinoid necrosis may be formed in the vessel in advanced cases, which can be seen primarily in haemorrhage cases. The accumulation of Aβ-40 peptides contributes to vascular deposition in arteries, capillaries, and veins. The proportion of vessels with Aβ deposits is primarily located in the occipital cortex, although their topography is variable. Type 1 cerebral amyloid angiopathy is described by the involvement of the capillary walls in a few cases of amyloid angiopathy. Type 1 cerebral amyloid angiopathy is associated with the alteration of the BBB due to the efflux of amyloid in the vessel. [37]

Crossing the BBB happens with the interaction between the Aβ peptide and the low-density lipoprotein receptor-related protein or p-glycoprotein. The transportation of Aβ across the BBB is affected by low-density lipoprotein receptor-related protein, which causes the efflux of Aβ from the brain into the blood. P-glycoprotein, an ATP-binding cassette transporter receptor, could be applied in Aβ clearance as an Aβ efflux pump at the BBB. A receptor for advanced glycation end products, a multi-ligand and cell surface receptor, is also a receptor that transports soluble Aβ across the BBB in the specific concentrations of plasma Aβ within the nanomolar range. Downregulating receptors for advanced glycation end products prevents the influx of Aβ. [38]

Neprilysin and insulin-degrading enzymes are one of the multiple enzymes that could scatter Aβ peptide. However, they are mostly cleared due to lymphatic vessels [37]. Neprilysin is a rate-limiting Aβ-degrading enzyme that degrades peptides at extracellular sites of Aβ deposits. Hence, decreased neprilysin levels and activity are seen in the cortex and hippocampus of the AD

brain. The insulin-degrading enzyme is also causing Aβ degradation in the brain. The levels of insulin-degrading enzyme decrease during ageing. In addition, it is more oxidised in the cortex and hippocampus than the cerebellum in the AD brain. Insulin-degrading enzyme also causes a malfunction in the Aβ proteolysis, which affects the Aβ accumulation in the cortical microvasculature of AD patients with cerebral amyloid angiopathy. [38]

Several aspects of the pathology Aβ, such as parenchymal and vascular deposits, are utilized in immunohistochemical reagents developed from anti-Aβ antibodies. Immunohistochemistry cannot detect the Aβ peptide from the brain of normal young adults. However, aging people or patients with, for example, familial AD or MCI are detectable due to increased Aβ deposition. The parenchymal Aβ deposits are associated with various proteins, lipids, and cells, such as ApoE, which is also involved in multiple other types of Aβ deposits. The production of ApoE is based on astrocytes in the brain. ApoE participates in cholesterol transport and is also a risk factor in AD. The immunoreactivity of diffuse Aβ deposits that also contain ApoE depends on the amount of quality of the immunohistochemistry. Amyloid deposits may include the Aβ-40 peptide and can be revealed by Aβ immunohistochemistry despite lacking the attributes of amyloid tinctorial. [37]

4.1.2.2 τ pathology

The accumulation of argyrophilic material in the cell body of neurons is associated with the production of neurofibrillary tangles (NFTs) based on neurofilaments. Although, the neurofilaments and tubulins were not the essential components for discovering NFTs, which was revealed by the anti-tau antibodies. T protein is a phosphoprotein containing a tubule binding domain consisting of three or four repeat regions (τ 3 R and 4 R). Isoforms of τ protein can be found in AD. Neurofibrillary lesions can be seen in various places within neurons, such as nerve cell bodies, apical dendrites as neurofibrillary tangles, distal dendrites as neuropil threads, and the abnormal neurites that relate to amyloid plaques. The development of neurofibrillary lesions in most nerve cells is related to the degeneration in AD. NFTs, neuritic plaque, and neuropil threads occur in the early stage of neurofibrillary degeneration. Hence, increased levels of CSF-τ from the abundance of neurofibrillary lesions correlate with the degree of dementia in elevated AD. [37], [39].

There are specific antibodies against various τ protein epitopes by labelling the NFTs with monoclonal antibodies, which are Alz50 and AT8. NFTs are found in multiple brain regions, primarily in the medium-sized pyramidal neurons of the hippocampus, the entorhinal cortex, and layers III and V of the isocortex. Even in the olfactory bulb, NFT can be detected early in the disease. However, extracellular NFTs are discovered in the entorhinal cortex and the pyramidal fields of the hippocampus, which could be the endpoint of neurofibrillary degeneration causing neuronal death. [37]

4.1.3 Treatments

Treatment of AD has a prior establishment for slowing the progression of the disease and making it easier to live with AD. The types of AD treatment are cholinesterase inhibitors, antioxidants, disease-modifying treatments, psychotropic agents, psychosocial interventions, and cognitive exercise. Decreasing the effect of the basic pathophysiology of AD by reducing amyloid production, aggregation of tau and Aβ, and enhancing the removal of amyloid production and NFTS in the brain are also prominent treatment for AD. [36]

Cholinergics are the nucleus basalis of Meynert supplied by basal forebrain neurons in the cerebral cortex. There is a connection between increased cholinergic dysfunction and cognitive dysfunction, where cholinergic treatment can stabilize cognitive decline in a few months. The most developed cholinergic treatment for mild to moderate AD is to use acetylcholinesterase inhibitors as medication. Acetylcholinesterase inhibitors slow AD progression by decreasing Aβ protein precursor, Aβ, and amyloidogenic production. Antioxidants can be used to slow the progression of AD. For instance, vitamins E and C can reduce the prevalence and incidence of AD. In addition, Estrogen enhances cerebral blood flow, prevents atrophy of cholinergic neurons, reduces oxidative stress, and reduces neuronal injury by decreasing the formation of Aβ. [40]

AD also creates behavioural symptoms during the progression, where treatment is based on nonpharmacologic techniques. For example, a patient needs a quiet and familiar environment to reduce disorientation and decrease aggressive behaviour. Positive and understandable language and reassuring the patient decrease aggressive behaviour [35]. For depressive symptoms, the patient is treated with selective serotonin reuptake inhibitors, such as tricyclic antidepressants, which may cause anxiety and irritability. Psychotropic medications have a significant role in treating behavioural disturbances in patients with AD. Studies suggest that the atypical antipsychotics risperidone and olanzapine affect treating psychosis and agitation in patients with AD [36].

4.2 Glymphatic system

The glymphatic system eliminates wastes and widely distributes glucose, lipids, amino acids, growth factors, and neuromodulators in the brain by a unique system of perivascular tunnels. The system is primarily formed on astroglia cells by increasing the efficient clearance of soluble proteins and metabolites from the central nervous system. The glymphatic system activates primarily during sleep. [21]

The glymphatic system comprises four brain fluid compartments: CSF, ISF, intracellular fluid, and blood vasculature. BBB and blood-CSF are based on brain parenchyma and CSF, which maintain the brain's extracellular environment. Brain parenchyma and CSF regulates the biochemical composition of the different fluid compartments. The subarachnoid space of the cortex and spinal cord drives the CSF through channels by four ventricles, which penetrate the brain parenchyma perivascularly. Hence, the CSF outflows from the brain to CNS and drives into the lymphatic systems. [21]

Blood vasculature produces the circulation between the brain and blood from cerebral arterial circulation, consisting of anterior and posterior cerebral circulation. Anterior and posterior cerebral circulation is supplied from the internal carotid arteries and the vertebral arteries. The anterior circulation perfuses evolutionary younger brain parts, including the hemispheres and neocortex. Simultaneously, the brainstem and the cerebellum are supplied by the posterior circulation. Cerebral circulation extends into pial arteries from cerebral arteries at the cortical surface by flowing through the CSF-containing subarachnoid and subpial spaces. Pial arteries are modified into penetrating arterioles in the brain parenchyma. Therefore, a perivascular space, known as the Virchow-Robin space, is based on a leptomeningeal cell layer on both the inner wall facing the vessel and the outer wall facing the perivascular astrocytic end part. [21]

Continuous exchange between the CSF and ISF is demonstrated in periarterial space by driving an influx of CSF to subarachnoid space. CSF flows into Virchow-Robin space by a combination of arterial pulsatility, respiration, and slow vasomotion. Polarisation of AQP4 water channels activates CSF pressure gradients. Due to the efflux of CSF into the parenchyma, ISF is driven into tissue toward the perivenous spaces surrounding the large deep veins. In the perivenous space, ISF is drained out of the brain toward the cervical lymphatic system, demonstrating the glymphatic system's function. [21]

Neurodegenerative diseases, such as AD, are characterized by the accumulation of aggregated proteins in the CNS, primarily during intracellular processes. Therefore, neurodegenerative disease impairs the glymphatic system. For instance, Apolipoproteins E and J produce high-density lipoprotein particles in astrocytes, which are associated with internal lipid transport in the brain. Apolipoprotein E production corresponds with CSF production sites and transport pathways by hindering the lipids transport in the glymphatic system. In addition, AD is associated with the depolarisation of perivascular AQP4 water channels. The depolarization of AQP4 water channels correlates with CSF–ISF exchange, which impairs the glymphatic system. [21]

4.3 FNIRS

FNIRS is a non-invasive technique in which brain tissue absorbs upcoming light and emits infrared light between 650 nm and 950 nm [33]. FNIRS is applied to monitor the brain hemodynamics of animals and humans. The benefit of using fNIRS is the high temporal resolution due to the higher sample rate and, in addition, being cheap diagnostic equipment. However, it has low spatial resolution due to the depth of the light wave by limiting penetration depth into the brain.

The development of fNIRS was promoted by multiple researchers. Beer-Lambert Law still described light absorption in homogeneous media [41], [42]. Felix Hoppe-Seyler, a German physician, discovered the absorption spectrum for hemoglobin and oxyhemoglobin [43]. The ability of hemoglobin to carry oxygen in the blood system was discovered by George Gabriel Stokes [43]. Karl von Vierordt was a biochemist who invented the techniques for measuring blood circulation by monitoring blood flow velocity and blood pressure [44]. Frans Jöbsis pioneered a non-invasive optical method of spectroscopy in 1977 [45], [46], which measures blood hemodynamics in the human brain by applying near-infrared light. He also proved the feasibility of non-invasive local spectroscopy of cortical tissue oxygenation through the intact skull [45], [46].

4.3.1 Theory

Light is emitted into the head at one specific position that undergoes random scattering and absorption processes in the tissue. Due to random scattering, the light travels along a banana-shaped path, not a straight line, from an emitter to a NIR-sensitive photodetector. The banana-shaped path is the product of the geometrical distance and differential path-length factor. There are a few data acquisition approaches for observing the fNIRS signal, such as continuous wave, frequency wave, and time wave domains. [41], [47]

In the continuous wave domain, the continuous light at constant amplitude is used to transilluminate the tissue by measuring the relative absorption of the attenuation amplitude over time. Continuous light is based on emitting discrete wavelengths or across the entire NIR spectrum. The variable time component is constant, making it exceedingly challenging to differentiate between light scattering and absorption effects due to slow or no modulation of the light. Continuous wave is a simple and flexible approach to gaining a high signal-to-noise ratio, but it produces a false signal due to superficial changes. [41], [47]

In the frequency wave domain, the light intensity is modulated multiple times at 10 – 100 MHz radio frequencies and then sent through the tissue. Photomultiplier tubes or fast photodiodes detect the signal, which provides attenuation and a phase shift φ concerning the incident signal. Differentiating between scattering and absorption effects is done by calculating the optical path length from the phase shift measurement. Hence, phase shift measurement provides a higher signal-to-noise ratio. [41], [47]

Short picosecond light pulses are broadened and attenuated in the time wave domain by the various tissue layers such as skin, skull, CSF, and brain. The temporal point spread function of the photons leaving the tissue describes the parameter changes in attenuation and the optical path length. The time wave domain does measure the absolute value of attenuation coefficients in scattering and absorption compared to the frequency wave domain technique. However, it is more expensive and demanding than the frequency wave domain system. [41], [47]

The path length of light extended because of scattering. Hence, the distance between the emitter and receiver is shorter than the path length of light, which is often around 30 mm. MBLL, not BLL, is applied to calculate the concentration of oxyhemoglobin and deoxyhemoglobin. There is a difference between MBLL and BLL, where BLL assumes the absolute optical densities providing absorption coefficients [41], [42]. However, in MBLL, the differential change in the optical density gives us a differential change in the absorption coefficient.

The approach of continuous wave fNIRS applies one or multiple light source-detector pairs and utilizes the MBLL:

$$A = ln\frac{I_{inc}}{I_{det}} = L\mu_a + G, \tag{1}$$

where A is the attenuation (defined here as logarithm base e), I_{inc} is the incident light intensity, I_{det} is the detected light intensity, L is the total mean path length of detected photons, μ_a is the absorption coefficient of the tissue, and G is a geometry-dependent factor. G is independent of absorption and represents intensity loss caused by scattering. **Equation 1** is corrected by calculating the average over the range of absorption coefficient $0–\mu_a$. Therefore, the differential form of the MBLL is not changed due to minor changes in attenuation. The absorption changes are homogeneous in the illuminated tissue volume by assuming the G as a constant variable

$$\Delta A = ln\frac{I_{det,1}}{I_{det,2}} = L\Delta\mu_a. \tag{2}$$

The attenuation change can be calculated from the detected intensity values of two different tissue states and is proportional to the absorption change (cf. **Equation 2**). **Equation 3** is the weighted sum of the change in the concentration of tissue chromophores, HbO and HbR:

$$\Delta\mu_a = \alpha_{HbO}\Delta c_{HbO} + \alpha_{Hb}\Delta c_{Hb}, \tag{3}$$

where the α weights denote the chromophores' specific (molar) absorption coefficients. If the attenuation change requires measured at two wavelengths, λ_1 and λ_2 (dual-wavelength measurement), and L can be measured or estimated, the concentration changes can be calculated as

$$\Delta c_{HbO} = \frac{\alpha_{Hb}^{\lambda_1} \frac{\Delta A^{\lambda_2}}{L^{\lambda_2}} - \alpha_{Hb}^{\lambda_2} \frac{\Delta A^{\lambda_1}}{L^{\lambda_1}}}{\alpha_{Hb}^{\lambda_1} \alpha_{HbO}^{\lambda_2} - \alpha_{Hb}^{\lambda_2} \alpha_{HbO}^{\lambda_1}}, \tag{4}$$

$$\Delta c_{Hb} = \frac{\alpha_{HbO}^{\lambda_1} \frac{\Delta A^{\lambda_2}}{L^{\lambda_2}} - \alpha_{HbO}^{\lambda_2} \frac{\Delta A^{\lambda_1}}{L^{\lambda_1}}}{\alpha_{HbO}^{\lambda_1} \alpha_{Hb}^{\lambda_2} - \alpha_{HbO}^{\lambda_2} \alpha_{Hb}^{\lambda_1}}.$$

For multiple wavelengths, measuring the concentration changes is applying linear least-squares fitting. [41], [47]

Equation 4 shows that the MBLL relies on two assumptions: the absorption of the medium changes homogeneously, and the scattering loss is constant [41]. However, the tissue absorption changes are spatially inhomogeneous in most practical cases. This reveals inaccuracy in the first assumption. Therefore, based on the first assumption, the MBLL formula has systematic errors of two kinds: the partial volume effect and crosstalk between chromophores. The partial volume effect depends on underestimating the changes in concentrations from applying the MBLL formula. The crosstalk between chromophores effect relies on the change in the concentration of other chromophores affecting the calculated concentration value in the MBLL formula [41], [47]. Incidentally, the second assumption also has a flaw, where the scattering loss changes the crosstalk of scattering into the estimated changes in chromophore concentrations. The scattering loss occurs when neuronal activation occurs in the brain or during the contraction of muscles. Hence, as outlined below, scattering corresponds to physiological processes in nervous tissue, where the light scatter is a measurement parameter [47].

The physiological parameters of fNIRS are derived from intrinsic optical signals. Receiving information from intrinsic optical signals is complicated due to various physiological events associated with multiple optical changes during brain activity. The various contributions to the intrinsic optical signals must be separated to understand optical signals regarding underlying physiological parameters. Intrinsic chromophores affect the absorption changes in biological tissue. Absorption changes in biological tissue are associated with concentration changes of different compounds from MBLL. Light absorption in endogenous chromophores depends on the functional state of endogenous chromophores, which can be measured from optical properties. Hence, the absorption spectrum of hemoglobin depends on its oxygenation state. The concentration changes in HbO and HbR controls the optical changes evoked by brain activity. Brain activity causes an increase in HbO and a decrease in HbR due to an increase in local cerebral blood flow. The increased focal blood flow causes temporary hyperoxygenation in the brain cortex, increasing oxygen consumption. Hence, the concentration changes of hemoglobins are associated with hyperoxygenation. [47]

4.3.2 Clinical applications

FNIRS is applied for studying sleep [32], traumatic brain injury [48], epilepsy [49], [50], cancer [51], [52], psychiatric disorders [53], and neurodegenerating disease such as AD [54]–[59] and Parkinson's disease [60], [61]. Multiple studies on AD by fNIRS relies on physical task such as verbal and visual task [57], [59], [62]–[66]. For instance, Hook et al. study investigates brain hemodynamics in verbal fluency task performance between AD patients and healthy subjects [59]. Hook et al. study demonstrated a decrease in cerebral blood flow and cerebral hemoglobin oxygenated in the parietal cortex in patients with AD compared to healthy controls [59]. Furthermore, Zeller et al. study provided results for detecting parietal activation deficits from AD patients with fNIRS, which indicates a possibility for an early detection method for AD [57]. In addition, few studies described fNIRS's ability to measure water dynamics from the brain, which is explained briefly in the following paragraphs [32], [33].

Myllylä et al. [33] conducted a study using fNIRS to investigate humans' brain water dynamics. In addition, a faster magnetic neuroimaging technique such as MREG was used to emphasise the connection between fNIRS and MREG. FNIRS measurements were based on 660, 830, and 980 nm. In conclusion, preliminary results provide that using 980 nm in combination with 830 and 660 nm or 740 nm allows the simultaneous sensing of dynamic variations in water volume and hemodynamics in the brain cortex. The correlation between H_2O and BOLD signal was good. [33]

Borchardt et al. [32] described fluctuations in cH_2O, HbO, HbR, and HbT (cerebral blood volume = total hemoglobin) during rest for 33 well-rested and 18 acutely sleep-deprived healthy control subjects. FNIRS signal was filtered in full-band, cardiac, respiratory, low-, and very-low-frequency bands. Results showed increased anti-correlation between fluctuation in concentrations of cH_2O and HbT across all frequency bands in both frontal and parietal cortices. In conclusion, the functional mechanism underlying glymphatic circulation in the human brain may be determined by observation of the anti-correlation between HbT and cH_2O. [32]

FNIRS and fMRI signals share similarities depending on hemodynamic response [67]. FMRI is based on a BOLD signal from neuronal activation [67]–[69]. FMRI measures cerebral blood volume and flow, which contains HbO and HbR due to the magnetic properties of hemoglobin. However, fNIRS can compartmentalize brain blood fluid compared to fMRI [67]. FNIRS measures the relative concentration of HbO and HbR. In addition, it can measure HbT by summing HbO and HbR. Hence, fNIRS can gain more detailed information about brain cortex hemodynamics than fMRI.

4.4 FMRI

FMRI is a safe, non-invasive, fast imaging system applied in clinical diagnosis and studies developed from MRI research. FMRI is based on BOLD signals and is used to study the physiological basis of brain hemodynamics, such as cerebral blood flow and cerebral blood volume. It has a high spatial resolution but a low temporal resolution.

Walter Gerlach and Otto Stern began detecting NMR in the 1920s by discovering the quantum nature of the silver atoms' magnetic moment [70]. Isidor Rabi proved the magnetic moments of the nuclei by measuring the single states of atoms and molecules' rotation [70]. Bloch and Purcell found the NMR signal [70]. Erwin L. Hahn developed a spin-echo method for gathering the effect of NMR into a gradient to study molecular diffusion in liquids [70]. FMRI developers were Paul C. Lauterbur and Peter Mansfield by localizing spatially NMR signals using magnetic field gradients [70]. Linus Pauling and his student, Charles Coryell, conducted studies to investigate the molecular structure of hemoglobin, and this provided HbO being diamagnetic and HbR paramagnetic [69]. Ogawa and his colleagues implied the BOLD mechanism, where neuronal activity causes changes in cerebral blood flow by increasing HbO and decreasing HbR [69]. They also showed that the BOLD signal has comparable properties with exogenous contrast agents but with better temporal resolution [69].

4.4.1 Theory

FMRI methods mainly depend on hydrogen protons being the signal source, whereas most human cells are water-based. Hydrogen is one of the candidate contrast mechanisms for functional brain imaging, including the local water concentration, transverse and longitudinal relaxation rates, and phase MRI signal. For instance, transverse and longitudinal relaxation rates form a basis for all common forms of fMRI in the local molecular environment by receiving properties of MRI relaxation times (T_1, T_2, and T_{2*}). Therefore, the alteration of relaxation time caused by local brain activity is associated with various physiological processes. The interactions between the magnetic moment and the local magnetic field are the source of NMR relaxation mechanisms. [69]

4.4.1.1 NMR signal

NMR excitation occurs when advancing from a lower to a higher energy state through radio frequency (RF) irradiation, which equals the splitting energy of spin states. RF energy relates to the local magnetic field (B) with a scaling factor depending on the nucleus of interest. The RF frequency (f) relates to the magnetic field strength due to the proportion between the energies of photons and their frequencies:

$$f = \frac{\gamma B}{2\pi}. \tag{5}$$

Equation 5 provides the resonance frequency (f) by exciting the system at certain energy states. Hence, the bulk magnetization vector moves from a longitudinal to a transverse magnetic field. [69]

RF excitation converts the magnetic field plane from longitudinal to transverse, which is detected through induction processes. Therefore, it causes the decay of spins at a different rate due to the local value of the magnetic field. Because of induced macroscopic magnetic fields within the sample, local magnetic fields have various imperfections in the magnet and the local molecular environments. In the transverse plane, the sum of the net magnetization vector is zero; the signal is undetectable due to randomization and readjustment of the spin population. The decay of transverse magnetization can be recorded as a function of time when the conducting loop generates an electrical current. The electrical current is digitized into a function of time by the NMR receiver, where the single RF pulse causes T_{2*}-decay. T_{2*} is based on the exponential time constant of the following signal decay. [69]

The reduction decay rate of transverse magnetization occurs due to a spin echo caused by a propagating second RF pulse to flip magnetization by 180° at a time halfway between the first RF pulse and the collection of signals. The phase of each spin is also reversed and accumulated for signal collection. The effect of the local magnetic field value is neglected due to a net relative phase being zero at the time of signal collection. Refocusing of heterogenetic magnetic fields is caused by a spin echo, which leads to a differentiation between T_2 and T_{2*}. Hence, T_2 is longer T_{2*} and causes signal decay on T_{2*} image because of being sensitive to magnetic field variations. [69]

The time scale for data collecting is based on the decay rate of transverse magnetization sets by RF excitation. Hence, T_2 (spin echoes) or T_{2*} (gradient echoes) is set to be the decays rate of transverse magnetization if the echo time (T_E) is referred to as the time between excitation and data collection,

$$M_T(T_E) = M_T(0)e^{-\frac{T_E}{T_2}}, \tag{6}$$

where M_T (0) is the initial value immediately following the RF excitation, and $M_T(T_E)$ is the value at the spin echo time. [69]

Relaxation time (T_1) s based on longitudinal magnetization. The thermal equilibrium of spins begins to stabilize after an excitation when the repopulation of the spin energy state is aligned with the magnetic field. As a result, the exponential recovery time of longitudinal magnetization starts from zero to the maximum value:

$$M_L = M_0\left(1 - e^{-\frac{t}{T_1}}\right). \tag{7}$$

Repeated excitations cause a steady value of longitudinal magnetization before each excitation, which depends on the repetition time (T_R) relative to T_1 and the flip angle of the RF pulse (α). The

amount of transverse magnetization is based on an excitation, which depends on the available longitudinal magnetization and the sine of the flip angle. The net T_1-dependent contribution to the signal is

$$M_L(T_R) = M_0 \frac{1 - e^{-\frac{T_R}{T_1}}}{1 - \cos\alpha\, e^{-\frac{T_R}{R_1}}} \sin\alpha. \quad (8)$$

The signal is at maximum in 90° flip angle when repetition times with $T_R << T_1$. The flip angle with shorter repetition times produces the maximum signal, the Ernst angle, which is calculated from $\cos\alpha_E = e^{-\frac{T_R}{T_1}}$. [69]

4.4.1.2 BOLD signal

BOLD signal is attributed to susceptibility changes in water proton spins inside and around the brain blood vessels caused by the local concentration of paramagnetic HbR. Local concentrations of paramagnetic HbR arise secondary to neuronal activation. Metabolism produces paramagnetic contrast agents, which influence T_2 as well as T_1 by shortening them. Shortening of T_2 or T_{2*} causes a signal loss due to the rapid decay of transverse magnetization. At the same time, the shortening of T_1 increases the signal due to the fast recovery of longitudinal magnetization following each excitation. Hence, blood magnetization is proportional to the stability of internal and external oxygen flow of a region. The rate of oxygen inflow is relative to cerebral blood flow. Increased cerebral blood flow decreases the amount of HbR contrast agent, which counters the effect of increased metabolism. [69]

BOLD contrast is contributed by many mechanisms [68]. The $T_{2'}$ effect is based on the dephasing of larger blood vessels. The Shortening of effective T_2 is caused by a dynamic average of smaller and intravascular vessels [68]. In addition, T_{2*}-contrast can describe every BOLD contrast mechanism, where the highest sensitivity level of BOLD is received from T_{2*}-weighted sequences. T_{2*} - weighted sequences are shown by assuming that the optimum echo time equals T_{2*}. T_{2*}-weighted sequences are included with an additional delay between excitation and signal acquisition, which decreases the sequences' efficiency. The sensitivity of T_{2*} is not optimal around the tissue of brain regions because of utilizing a single delay for T_{2*}-weighting [68]. The measured signal from T_2 or T_2* contrast mechanisms is proportional to a degree of spin coherence within the volume due to the spin's precession. Spin's precession generates a relation between frequency and the local magnetic field. Hence, non-isotropic field disturbances will cause signal loss due to loss of coherence [69].

4.4.1.3 Physiological of BOLD signal

Understanding the physiology of the BOLD method is essential for applying fMRI. BOLD is well known that neuronal activity is based on metabolic energy achieved from achieving the substrates delivered by blood flow, which is reflected on the changes of the HbR level. Changes in the HbR level are caused by the metabolic consumption rate of oxygen, blood flow, and blood volume [68]. Unfortunately, the descriptions of metabolic requirements and pathways still need to be discovered and their subsequent transduction into the hemodynamic response [69].

Neural activity is produced by postsynaptic neuronal depolarisation and the action potential generation. The transportation of information and its integration postsynaptically cause most of the energy consumption. Hence, local blood flow increases because of the increase in substrate transportation for energy metabolism. However, the increased local blood flows are driven by the consequence of neurotransmitter action, which reflects the local signalling, and not from the increased metabolic energy. The correlation between change in the local field potential and increased BOLD signal is apparent and increased in energy production. Therefore, a decrease in oxygen extraction depends on neuronal activity [69], [71]. The association between increased local blood flow and neuronal activity is determined by the level of perfusion local control by feeding arterioles. Nitric oxide and eicosanoids are a few of the multiple mediators of the arterioles. These mediators may control the vascular response of glial cells around synapses by releasing nitric oxide, which is triggered by glutamine binding to its receptors. [71]

The increased neuronal activity causes a reduction in oxygen extraction, which leads to an increased HbO and HbR ratio in the blood flow. Hence, the HbO and HbR ratio in the blood flow is associated with the BOLD signal, where the changes lie in the different magnetic properties of HbO and HbR. HbR and capillaries have paramagnetic magnetic properties in brain tissue. Blood distorts the magnetic field in their proximity due to the orbital motion of the electrons producing an aligning magnetic field. HbO has diamagnetic properties, where the blood causes minimal or neglectable distortion in the magnetic field due to the orbital motion of the electrons producing a conflicting magnetic field. HbR causes destructive interference signals within a tissue voxel by affecting the microscopic field inhomogeneities. This process shortens the T_{2*} relaxation time, where oxygen extractions decrease in increased local blood flow due to neuronal activity. Hence, the increment of fMRI signal intensity is proportional to the HbO and HbR ratio. [69], [71]

The increment of fMRI signal intensity depends on an intravascular and extravascular compartment [69], [71]. The intravascular compartment describes the movement of water molecules in the blood. The extravascular compartment describes the movement of water molecules in the tissue space around the vessels. The fMRI signal is produced by a volume-weighted averaged signal, which relies on the water in the intravascular and extravascular compartments [69], [71]. Hence, the fMRI signal intensity is proportional to the changes in cerebral blood volume. Hypo-oxygenation leads to decreased fMRI signal intensity due to decreased metabolism [68]. In hypo-oxygenation, blood oxygenation decreases, and the cerebral blood volume is mainly based on HbR. The increased fMRI

signal intensity is led by hyperoxygenation. Hyperoxygenation is based on increased blood oxygenation, whereas cerebral blood volume is based mainly on HbO [68].

4.4.2 MREG

Echo planar imaging is one of the fMRI methods, whereas the temporal resolution for whole brain imaging is around 2-3 s. Although, higher temporal resolution is necessary for measuring a single event hemodynamic response function lasting approximately 20 s. Therefore, the MREG sequence is applied for higher temporal resolution than echo planar imaging. Standard echo planar imaging protocol measures ten data points during this time period, while MREG achieves 200 data points in the same period. The benefit of the fast acquisition allows a better analysis of the onset and shape of the hemodynamic response function, improved statistical power, and the ability to distinguish respiration and cardiac frequencies by direct filtering. Spatial encoding in MREG is achieved by combining a small amount of gradient encoding with the spatial information from multi-coil arrays. [72]

A few projections for 2D functional imaging or a rosette k-space trajectory for single-shot 3D are techniques for spatial encoding in MREG. The complexity of non-Cartesian trajectories derives from the off-resonance behaviour. The off-resonance behaviour causes complications to rosettes and single-shot radial trajectories by being overly sensitive due to off-resonance, T_{2*} - decay, and gradient imperfections. Correction for off-resonance behaviour relies on concentric shells, which do not have an intersection. K-space sampling is symmetrical and gains higher spatial-temporal resolution due to permitting longer readout times. Hence, point spread functions do not display off-resonance dependent shifts and consequently no image distortions due to symmetry. However, blurring and signal dropout are caused by off-resonance. Blurring is harder to correct compared to geometric distortions, which can be corrected with suitable co-registration procedures. A single shot stack of spirals technique is applied to maintain echo planar imaging off-resonance behaviour. The single shot stack of spirals technique is based on sampling the k-space monotonously from the beginning point to the end in variable-sized steps. Following the slow encoding direction, each step acquires a variable density spiral at one of the Cartesian k-space coordinate axes. The benefits of the single shot stack of spirals technique are fast acquiring each spiral and avoiding appreciable artifacts in other directions. [72]

The k-space trajectory consists of twenty-one spirals engraved within a sphere. The distance between spirals and the k-spaces increases by sampling individual spiral elements with variable density. The 64-channel head coil is used for MREG data acquisition, where the brain is covered with forty coils of the head coil. Data reconstruction begins with iterative under sampling of the data, the volume size of 64x64x64, and with a factor around 1.8 or 2.6 per direction. Due to highly iterative reconstruction, the actual spatial resolution is lower and anisotropic compared to the nominal spatial resolution, which is 3 mm and isotropic. Hence, regularized reconstruction is applied. Walsh's method is applied to calculate the coil sensitivities from the data after calculating the field map of coil images. Walsh's method combines voxel-wise with the maximum intensity of absolute values over all coils from phase differences between two echoes. Finally, the DORK

("dynamic of-resonance in k-space") is applied to alter frequency changes during data acquisition by correcting field inhomogeneities based on the separately acquired field map. [72], [73]

4.4.3 Clinical applications

The increased number of fMRI studies provides a variety of applications for the diagnosis and development of new therapies. Although, the clinical research applications for fMRI are limited to the brain area. Therefore, it is based on understanding the development of the normal or pathological brain, such as cognition or the characterization of disease, and dynamic functional neuropathology, for example, epilepsy and dementia diseases. [68]

With fMRI, it is possible to enable safer presurgical localization of critical functional regions in the brain. For example, the use of fMRI in epilepsy surgery is increased because the information about the epilepsy brain from the fMRI signal displays the potential brain regions for epileptic seizures. In addition, fMRI can also be used in sizeable surgical series such as language and memory lateralization for robust support. Investigating the localization of memory functions in a patient before surgery described verbal and visual memory decline better than preoperative conventional neuropsychological assessments in a memory task. Hence, showing the correlation between fMRI activation and localization in the brain is a beneficial and efficient method for studying brain structures. FMRI can also be applied while measuring brain activity in a patient's cognitive and behavioural state during an injury or a treatment. [68]

For gaining functional connectivity and hemodynamics from the brain, the MREG sequence is used because of being a faster sequence than the conventional scanning sequence, such as the echo planar imaging sequence. With MREG, three physiological brain pulsations are distinguishable from the signal: cardiac pulsation, respiratory pulsation, and vasomotor pulsation. Cardiorespiratory pulsation was regarded as noise for being inconvenient in spontaneous brain activations in the BOLD signal, where vasomotor waves are related to spontaneous functional connectivity fluctuations. Hence, heart rate variability and respiration are associated with causing modulation of cognitive performance and brain activation responses. Measuring variability of the MREG signal correlates with pathological AD, since it is altered in AD. Another method for measuring the variance of the cardiovascular pulsation from MREG is called optical flow. It is based on calculating the velocity propagation of cardiovascular brain impulses. The optical flow method detected altered variance in the propagation of cardiovascular brain impulses and abnormalities in the directionality and magnitude of brain pulsations in AD. In addition, MREG can be applied on epilepsy studies by detecting the alteration of respiratory pulsation in patients. [73]

5 MATERIALS AND METHODS

5.1 Subjects

Subjects	Amount (females)	Age	MMSE
AD	16 (8)	57.8 ± 4.0	23.4 ± 6.5*
Controls	16 (11)	59.8 ± 5.4	28.1 ± 1.4*

Table 1. Participants of the study, where * shows statistical differences with $p < 0.05$.

Thirty-two subjects participated in the study, where 16 (8 females) AD patients aged 57.8 ± 4.0 and 16 (11 females) healthy controls aged 59.8 ± 5.4 (cf. **Table 1)**. The current National Institute of Neurological and Communicative Disorders and Stroke and the Alzheimer's Disease and Related Disorders Association diagnosis criteria for probable AD were met by the AD patients. Furthermore, subjects underwent multiple examinations, such as clinical and neurological examinations, laboratory screening tests, neuropsychological examinations, and brain images from structural and functional MRI. In addition, diagnosed AD patients gave their CSF samples for analysis of the biomarkers, Aβ42, τ, and phospho-τ, and engaged metabolic neuroimaging by fluorodeoxyglucose positron emission tomography. In addition, MMSE examinations for estimating cognitive impairment were conducted to age-matched control subjects (28.1 ± 1.4) and AD patients (23.4 ± 6.5) (cf. **Table 1)**. Significant differences ($p = 0.01$) were detected between AD patients and healthy controls. The healthy control group was limited to people with no history of psychiatric or neurological disorders or recent use of medications affecting the central nervous system. The Northern Ostrobothnia Hospital District Regional Ethics Committee approved this study, which was conducted per the Declaration of Helsinki. The participants or their caretakers gave their written informed consent to be involved with the study.

5.2 Measurements

All subjects were scanned using a Siemens Skyra 3 T MRI scanner (Siemens Healthineers AG) with a 32-channel head coil equipped with an MREG sequence from Freiburg University. MREG is a single-shot three-dimensional (3D) sequence, which utilizes a spherical stack of spirals and undersamples the 3D k-space trajectory [72]. This study used the following sequence parameters: repetition time = 100 ms, echo time = 36 ms, the field of view = 192 mm, voxel size = 3 mm, and flip angle = 25° [24], [74]. The reconstruction of MREG data was based on L2-Tikhonov regularisation with $\lambda = 0.1$. The L-curve method determined the latter regularisation parameter, where the resulting spatial resolution was 4.5 mm FWHM. Furthermore, continuous image MREG reconstruction was done with DORK ("dynamic off-resonance in k-space") method, which corrects scanner warming and respiration-induced dynamic B_0-field changes [24], [74]. By obtaining anatomical high-resolution T_1-weighted MPRAGE (repetition time = 1900 ms, echo time = 2.49 ms, inversion time = 900 ms, flip angle = 9°, field of view = 2,40 and slice thickness = 0.9 mm) images,

MREG was co-registered with data to each subject's anatomy, and followed by resampling into the T_1 Montreal Neurological Institute (MNI 152) 4 mm standard space [24], [74].

During the 5 min MREG resting state study of 2961 volume frames, the subject was instructed to lie still in the scanner with their eyes open while fixating their gaze on a cross on a video monitor. The subjects were fitted with soft pads and ear plugs to minimize head motion and dampen auditory stimuli during the study. In addition, fNIRS probes were installed into the subject's forehead to gain simultaneous MREG measurements (cf. **Fig. 5-2a**). [33], [75]

FNIRS device was built at the University of Oulu in cooperation with Oulu Functional Neuroimage (OFNI) and Optoelectronics and Measurement Techniques (OEM) research units [34]. The device consists of two types of light sources to gain specific infrared radiation: laser diode for 980nm and high-power light-emitting diodes for 660 nm, 740 nm, and 830 nm. The light of each light source was modulated for the specific frequency, directed into one fibre bundle, and then on the scalp. The detector received attenuated light. Then the signal from the detector continues to the amplifier, where the signal is then demodulated [32]–[34], [75]. One fNIRS channel was positioned on the left forehead above the eye. 660 nm, 830 nm, and 980 nm fNIRS wavelengths have been used in the analysis of this study. The fNIRS technique used a frequency-coded system. The frequency-coded technique applied the measurement of attenuation, the backscattered light phase from the tissue, and the modulation of illuminating light intensity for enhancing the fNIRS signal [33]. FNIRS device decreases the signal's noise by using a very narrow bandwidth filter and the lock-in amplification technique [33]. The sample rate on the device was 10 kHz, but it was downsampled into 10 Hz for a comparison with the MREG data [33], [75].

5.3 Data processing

The FSL pipeline was operated during pre-processing of the MREG data. Minimizing the T1-relaxation effects on the data was high-pass filtered with a cut-off frequency of 0.008 Hz (125 s) and 80 time points (8 s) from the beginning of the time series were removed [23], [24], [74]. Next, FSL MCFLIRT was conducted for motion correction to the MREG data. FSL BET was used for brain extraction with the following parameters: fractional intensity = 0.1–0.25, threshold gradient = 0.1–0.22, with neck and bias-field correction option. Spatial smoothing was conducted using a 5 mm FWHM Gaussian kernel [23], [24], [74]. *FSLeyes* drew region-of-interest at the fNIRS probe area (cf. **Fig. 5-2b**). *Fslmeants* was applied to calculate the average signal from the region-of-interest voxels of the fNIRS probe area. Finally, the MREG data were bandpass filtered into the cardiac frequency band (0.6-5 Hz) [24] and normalized at a range of [0,1] (cf. **Fig. 5-2c**).

FNIRS data was despiked by interpolation [76] and detrended. MBLL was used to calculate the concentration of HbO, HbR, and H_2O with the optical density values and extinction coefficients of each wavelength, and the differential path length factor, which was 5.93 [41], [77]. The extinction coefficients were for 660 nm: HbR: 3.4408, HbO: 0.3346, H_2O: 0.0166; for 830 nm: HbR: 0.7804, HbO: 1.0507, H_2O: 0.1459; and for 980 nm: HbR: 0.4233, HbO: 1.2513, H_2O: 2.1491 [77]. HbT was calculated by summing the HbO and HbR. Finally, the fNIRS data were bandpass filtered into the cardiac frequency band (0.6-5 Hz) [24] and normalized at a range of [0,1] (cf. **Fig. 5-2c**).

5.4 CBP

Overall pulse amount	Control	Alzheimer
Type A		
HbO	1448	1231
HbR	1509	1514
HbT	1220	1199
H_2O	1362	1327
MREG	801	1055
Type B		
HbO	1133	1319
HbR	1154	1349
HbT	1480	1316
H_2O	1225	1170
MREG	1103	832
Type C		
HbO	1142	1384
HbR	1473	1323
HbT	1101	1313
H_2O	1145	1247
MREG	1176	933
Type D		
HbO	3723	3934
HbR	4135	4186
HbT	3801	3828
H_2O	3732	3744
MREG	3080	2820

Table 2. Overall pulse amount was analysed from diverse CBP types of AD patients and healthy controls using recorded fNIRS and MREG data.

Analysing and defining the CBP was done with a few steps in MATLAB. The first step was to detect pulses by finding the pulse peak, beginning and end points of pulse in the cardiac frequency-filtered signal using *the findpeaks* – command. A few input arguments were defined before applying the findpeaks – command to enhance the pulse detection in the cardiac frequency-filtered data. These were the minimum peak height and distance. The minimum peak height was the calculated mean root square value from the data. The minimum peak distance was the sum of heart rate data and the data's sample rate. The heart rate was defined by measuring the cardiac frequency-filtered data's maximum power spectrum value. The examples of pulse peaks in the cardiac frequency-filtered data can be seen in **Fig 5-2c)**.

The next step was to define the nature of the CBP with the five distinct parameters: PD, PRD, PFD, PA_1 and PA_2. PD describes the duration of a pulse. PRD describes the duration from the beginning of a pulse to the pulse peak. PFD describes the duration from the pulse peak to the end of a pulse.

PD, PRD and PFD relied on the data of the recorded time points, where each time point was equal to 0.1 seconds due to the sample rate of fNIRS and MREG.

After defining the PD, PRD and PFD, the shape of the pulse was enhanced by modified Akima cubic Hermite interpolation up to 100 data points. This was necessary because of fewer data points in the original pulse. Therefore, determining PA_1 and PA_2 was distinguishable by assuming the shape of the interpolated pulse as a rectangular triangle. The rectangular triangle is based on PD, PRD and PFD from the interpolated pulse. PD is the hypotenuse of a rectangular triangle. PRD is the first height of the rectangular triangle. PFD is the second height of a rectangular triangle, where PRD and PFD create a 90-degree angle. Hence, calculating PA_1 and PA_2 was done with trigonometry. PA_1 was calculated as a cosine between the values of PRD and PD. PA_2 was calculated as a cosine between the values of PFD and PD.

After determining PA_1 and PA_2, the pulses were divided into four CBP type groups: types A, B, C and D. The pulse was categorized as Type A (cf. **Fig. 5-1, Table 2.**) if PA_1 was between 50 and 90 degrees, PA_2 was between 0 and 40 degrees, and the PRD was shorter than the PFD. The pulse was categorized as Type B (cf. **Fig. 5-1, Table 2.**) if PA_1 was between 0 and 40 degrees, PA_2 was between 50 and 90 degrees, and the PRD was longer than PFD. The pulse was categorized as Type C (cf. **Fig. 5-1, Table 2.**) if the pulse was not classified as either Type A or Type B. Finally, type D (cf. **Fig. 5-1, Table 2.**) is the sum of Type A, B and C.

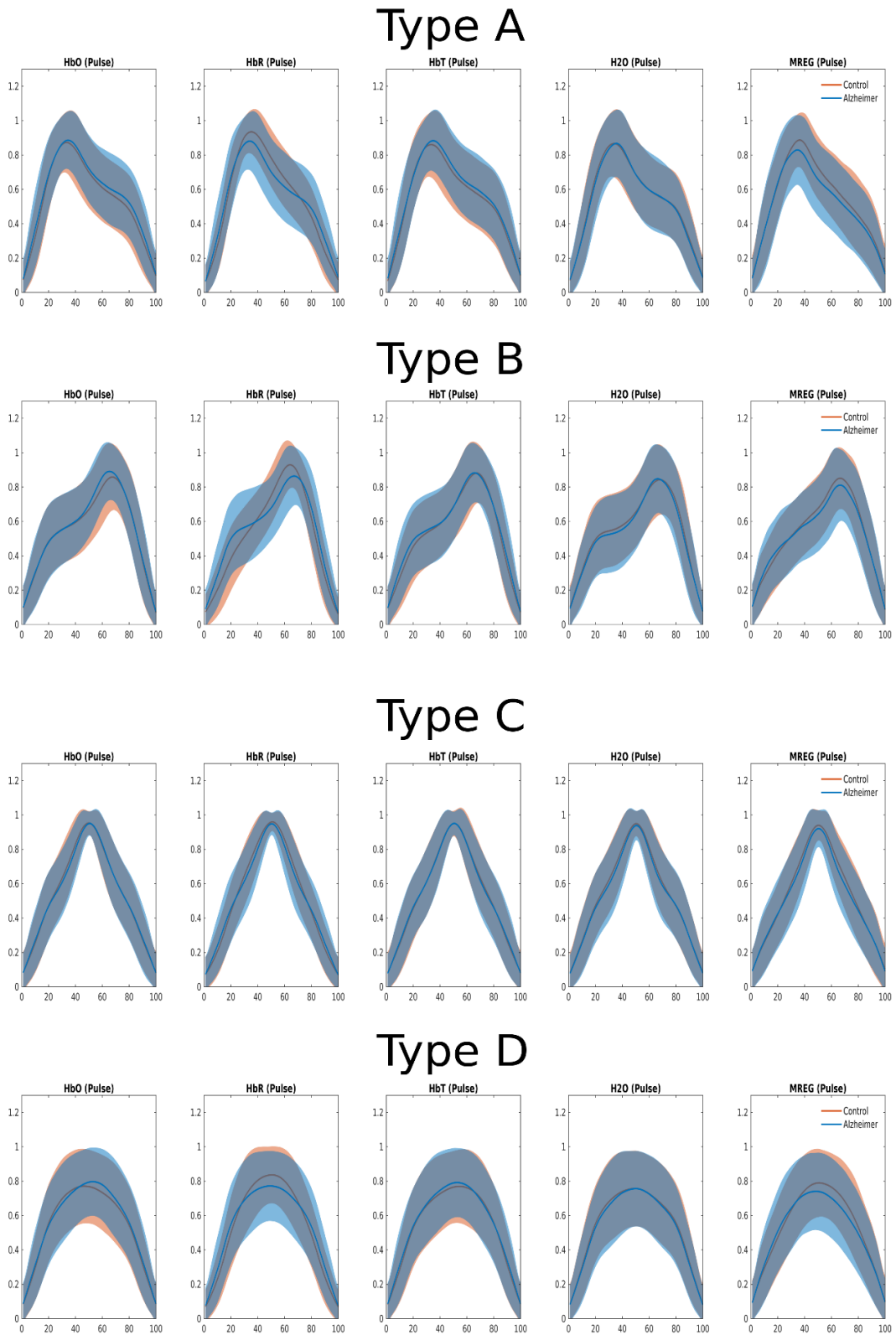

Figure 5-1. Calculated averages (the bulked lines on the plots) and standard deviations (shaded area of the bulked line) of diverse CBP types of AD patients and healthy controls on the basis of fNIRS and MREG data. The X-axis represents the number of data points of the interpolated pulse, and the Y-axis describes the normalised CBP range.

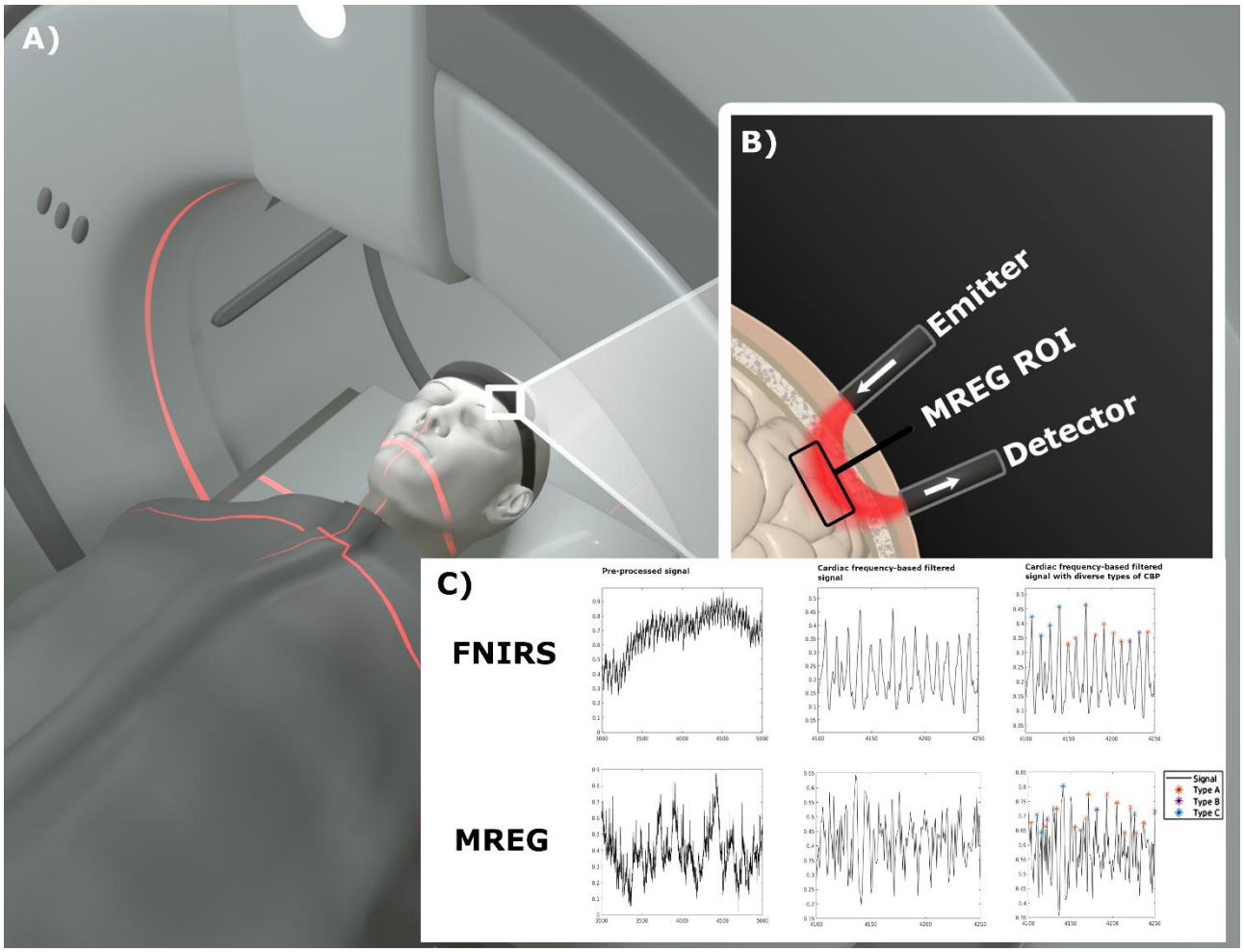

Figure 5-2. Methodology of the study. A) describes the principle of the study, where the subject was lying on the table while the fNIRS device was on the forehead. Then, B) describes the principle of fNIRS, where the red-coloured banana-shaped area covers the light movement from emitter to detector. In addition, the MREG region-of-interest (ROI) voxels were gathered from the red-coloured banana-shaped area to gain simultaneous imaging between MREG and fNIRS. Finally, C) shows the pipeline of defining diverse CBP types with the parameters obtained from MREG and fNIRS signals of a healthy control: the pre-processed signal (left), cardiac frequency-based filtered (middle) and diverse types of CBP (right).

5.5 Statistical analysis

A nonparametric randomization test (*permutationTest* function in Matlab Laurens R Krol, Permutation Test (https://github.com/lrkrol/permutationTest), GitHub. Retrieved January 20, 2022) was used for statistical analysis [78]. Randomization test is a statistical test that measures the statistical difference between the means of the two groups by providing a p-value and effect size, which was based on Cohen's *d* effect. Effect size describes the direction of the impact, which correspond to the strength of the relationship between two variables in a population. For instance, if M1 is the experimental group and M2 is the control group, a negative effect size indicates that the

effect decreases M1's mean. Conversely, a positive effect shows that the effect increases M1's mean. Furthermore, the results were corrected with a false discovery rate by multiple comparison tests of Benjamin-Hochberg, where a p-value < 0.05 was declared significant [79].

6 RESULTS

The first step was to verify the differences in diverse CBP types between AD and healthy controls when simultaneously using two independent imaging methods. If both methods detected similar changes in diverse CBP types, the simultaneously detected results with independent methodology would cross-verify the existence of pathological changes during AD in the case of both methods. It was also considered to detect comparable results with a change in AD between MREG and fNIRS brain fluid compartment, HbO, HbR, HbT and H_2O, from diverse CBP types. CBP parameters are PD, PRD, PFD, PA_1 and PA_2 from MREG and fNIRS filtered signals within cardiac frequency (0.6 - 5 Hz). In addition, the pulse amount of diverse CBP types of AD patients and healthy controls. Both methods detected statistical differences in CBP parameters between AD patients and healthy controls on each CBP type.

6.1 Pulse amount

Mean ± SD	Control	Alzheimer		
Type A	Pulse amount	Pulse amount	P-values	Effect size
HbO	91 ± 39	77 ± 39	0,6011	-0,286
HbR	94 ± 49	95 ± 49	0,9867	0,005
HbT	76 ± 42	75 ± 41	0,9737	-0,028
H_2O	85 ± 36	83 ± 35	0,9437	-0,048
MREG	50 ± 16	66 ± 17	**0,0230**	**1,024**
Type B				
HbO	71 ± 38	82 ± 38	0,6598	0,245
HbR	72 ± 44	84 ± 44	0,7374	0,194
HbT	93 ± 41	82 ± 41	0,7373	-0,195
H_2O	77 ± 41	73 ± 36	0,8968	-0,088
MREG	69 ± 16	52 ± 16	0,1228	-0,707
Type C				
HbO	71 ± 40	87 ± 41	0,4678	0,370
HbR	92 ± 50	83 ± 44	0,7249	-0,200
HbT	69 ± 33	82 ± 40	0,4750	0,360
H_2O	72 ± 36	78 ± 35	0,7528	0,180
MREG	74 ± 24	58 ± 25	0,1830	-0,621
Type D				
HbO	233 ± 92	246 ± 75	0,7825	0,157
HbR	258 ± 95	262 ± 51	0,9652	0,042
HbT	238 ± 75	239 ± 75	0,9777	0,021
H_2O	233 ± 78	234 ± 77	0,9867	0,010
MREG	193 ± 50	176 ± 46	0,5061	-0,339

Table 3. Calculated average (Mean) and standard deviation (SD) of diverse CBP types of AD patients and healthy controls on the basis of pulse amount of fNIRS and MREG data. Bolded numbers are statistically significant results ($p < 0.05$).

The pulse amount results showed a significant difference in type A from MREG, where the pulse amount was increased in AD patients (50 ± 16 vs 66 ± 17, $p < 0.05$, $d = 1.024$) (cf. **Fig. 6-1, Table 3.**). FNIRS results showed no significant difference in pulse amount between AD patients and healthy controls.

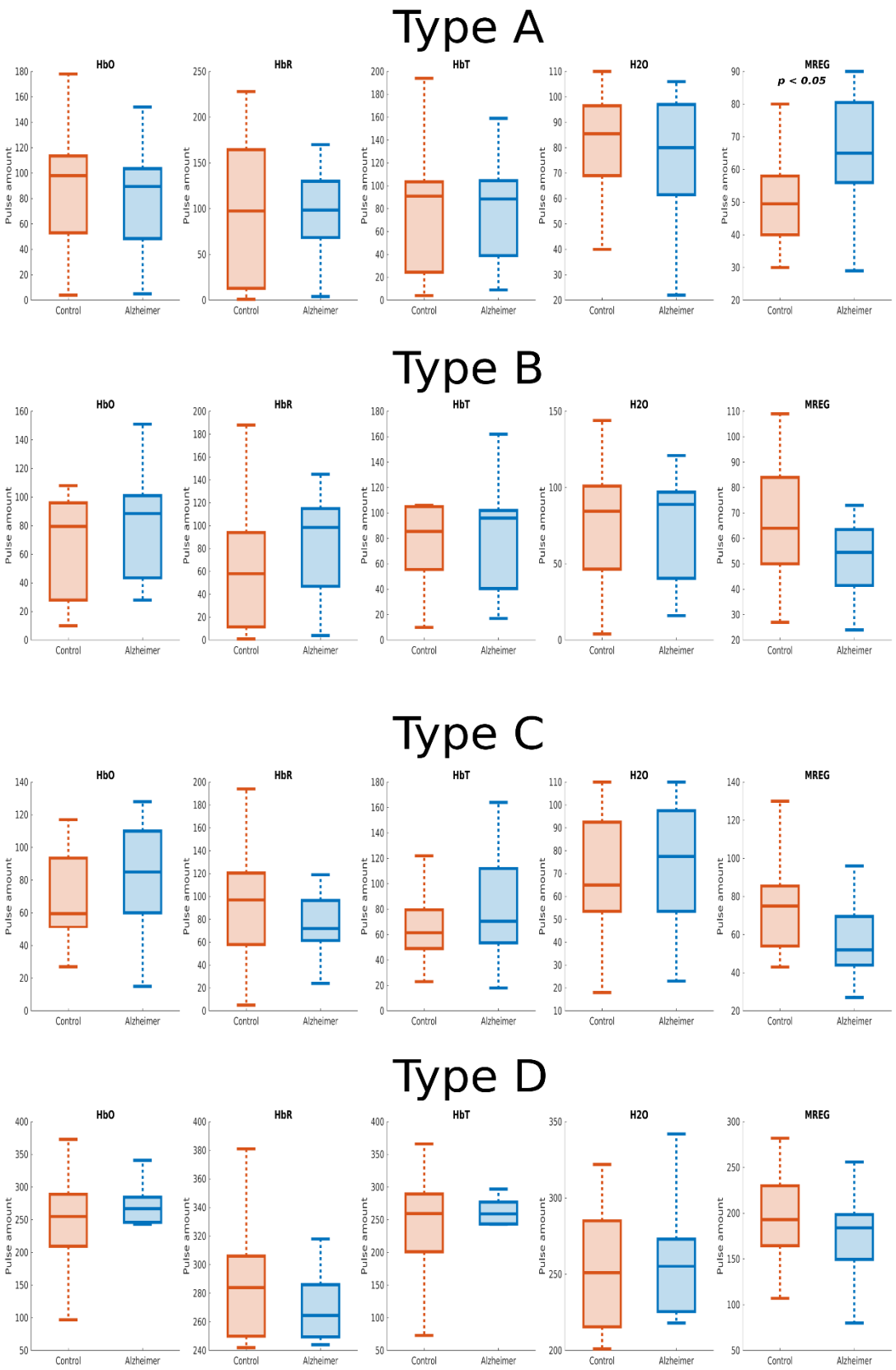

Figure 6-1. Boxplots of the properties of diverse CBP types of AD patients and healthy controls calculated on the basis of the pulse amount of fNIRS and MREG data. The only statistically significant results are marked above the boxplot in question.

6.2 PD

Mean ± SD	Control	Alzheimer		
Type A	PD	PD	P-values	Effect size
HbO	10.8 ± 2.6	11.0 ± 2.5	**0,0261**	**0,102**
HbR	10.7 ± 1.8	10.9 ± 2.2	**0,0107**	**0,110**
HbT	11.2 ± 2.8	10.8 ± 2.6	**0,0026**	**-0,148**
H_2O	11.2 ± 2.7	11.0 ± 2.6	0,2352	-0,061
MREG	12.5 ± 3.8	12.1 ± 3.8	0,1684	-0,082
Type B				
HbO	11.2 ± 2.6	10.9 ± 2.6	0,0584	-0,094
HbR	10.4 ± 2.3	11.0 ± 2.3	**0,0007**	**0,300**
HbT	10.8 ± 2.7	11.4 ± 2.7	**0,0007**	**0,231**
H_2O	11.2 ± 2.7	11.2 ± 2.7	0,9254	-0,007
MREG	12.7 ± 3.7	13.1 ± 3.7	**0,0237**	**0,125**
Type C				
HbO	10.7 ± 2.8	10.9 ± 2.4	0,1008	0,083
HbR	10.5 ± 2.2	10.9 ± 2.3	**0,0007**	**0,188**
HbT	10.7 ± 2.8	11.1 ± 2.5	**0,0135**	**0,124**
H_2O	11.0 ± 2.8	11.1 ± 2.6	0,1830	0,070
MREG	11.1 ± 2.8	11.7 ± 3.1	**0,0007**	**0,205**
Type D				
HbO	10.9 ± 2.7	10.9 ± 2.5	0,3119	0,031
HbR	10.5 ± 2.1	11.0 ± 2.3	**0,0007**	**0,196**
HbT	10.9 ± 2.8	11.1 ± 2.6	**0,0080**	**0,073**
H_2O	11.1 ± 2.8	11.1 ± 2.6	0,9652	-0,002
MREG	12.0 ± 3.4	12.3 ± 3.6	**0,0126**	**0,077**

Table 4. Calculated average (Mean) and standard deviation (SD) of diverse CBP types of AD patients and healthy controls on the basis of PD of fNIRS and MREG data. One timepoint correspond to 0.1 second due to the sample rate of fNIRS and MREG. Bolded numbers are statistically significant results ($p < 0.05$).

FNIRS parameters detected a significant difference in PD of type A. The PD of HbO and HbR were increased in AD patients (HbO: 10.8 ± 2.6 vs 11.0 ± 2.5, $p < 0.05$, $d = 0.102$; HbR: 10.7 ± 1.6 vs 10.9 ± 2.2, $p < 0.05$, $d = 0.110$). However, in HbT, the PD was decreased in AD patients (HbT: 11.2 ± 2.8 vs 10.8 ± 2.6, $p < 0.01$, $d = -0.148$). MREG and FNIRS showed increased PD of type B in AD patients (MREG: 12.7 ± 3.7 vs 13.1 ± 3.7, $p < 0.05$, $d = 0.125$; HbR: 10.4 ± 2.3 vs 11.0 ± 2.3, $p < 0.001$, $d = 0.231$; HbT: 10.8 ± 2.7 vs 11.4 ± 2.7, $p < 0.001$, $d = 0.300$). Both methods detected a significant difference in PD of type between AD patients and the healthy controls. PD was increased in AD patients (HbR: 10.5 ± 2.2 vs 10.9 ± 2.3, $p < 0.001$, $d = 0.188$; HbT: 10.7 ± 2.8 vs 11.1 ± 2.5, $p < 0.001$, $d = 0.124$; MREG: 11.1 ± 2.8 vs 11.7 ± 3.1, $p < 0.001$, $d = 0.205$). Furthermore, both methods detected increased PD of type D in AD patients (HbR: 10.5 ± 2.1 vs 11.0 ± 2.3, $p < 0.001$, $d = 0.196$; HbT: 10.9 ± 2.8 vs 11.1 ± 2.6, $p < 0.01$, $d = 0.073$; MREG: 12.0 ± 3.4 vs 12.3 ± 3.6, $p < 0.05$, $d = 0.077$). The PD results were shown in **Table 4.** and **Fig 6-2**.

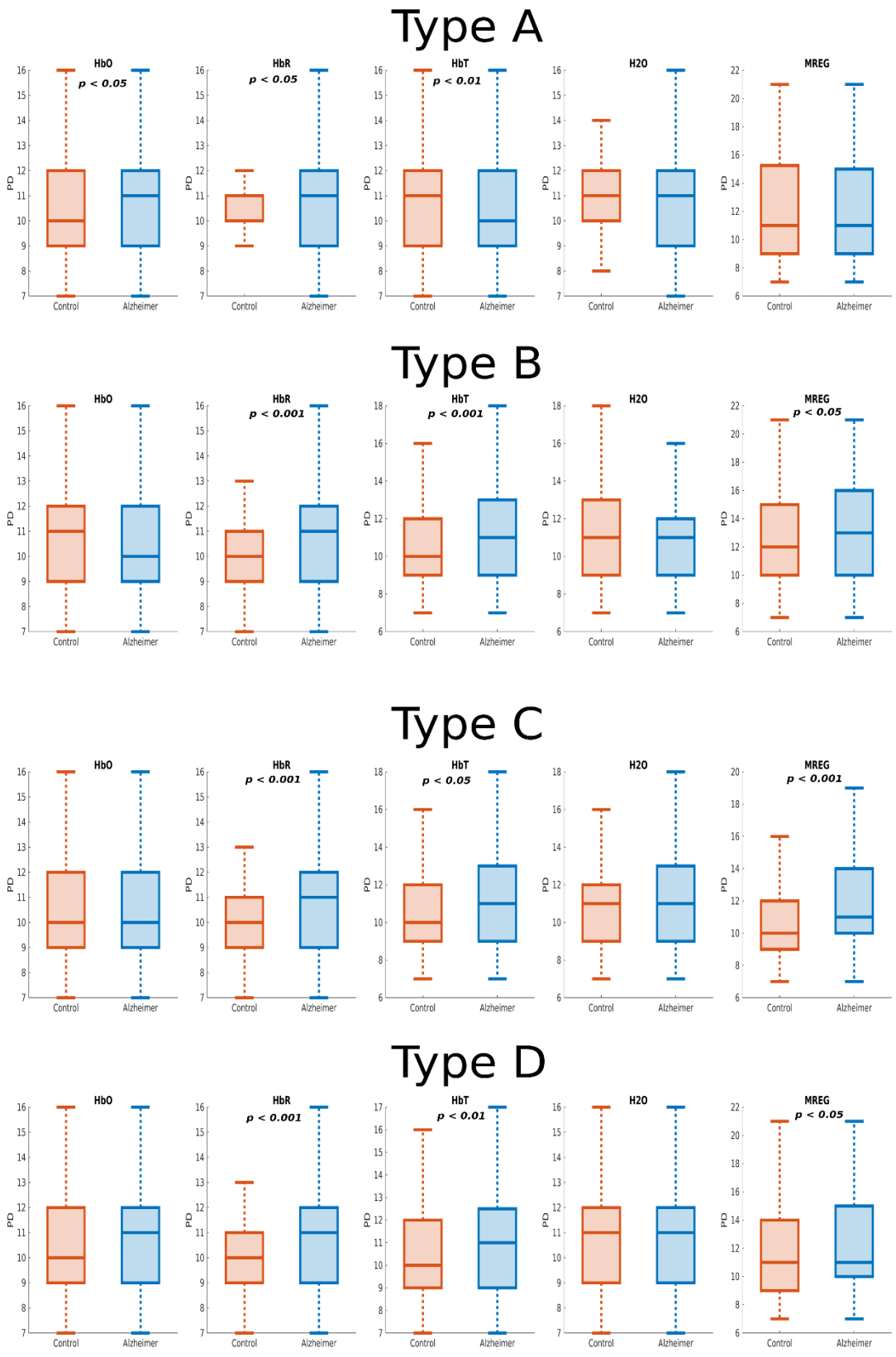

Figure 6-2. Boxplots of the properties of diverse CBP types of AD patients and healthy controls calculated on the basis of the PD of fNIRS and MREG data. One timepoint correspond to 0.1 second due to the sample rate of fNIRS and MREG. The only statistically significant results is marked above the boxplot in question.

6.3 PRD

Mean ± SD	Control	Alzheimer		
Type A	PRD	PRD	P-values	Effect size
HbO	4.1 ± 1.1	4.2 ± 1.1	0,0564	0,090
HbR	4.3 ± 0.9	4.2 ± 1.2	**0,0026**	**-0,125**
HbT	4.2 ± 1.2	4.1 ± 1.1	0,5471	-0,036
H_2O	4.2 ± 1.1	4.2 ± 1.1	0,8968	-0,010
MREG	4.7 ± 1.5	4.4 ± 1.6	**0,0007**	**-0,244**
Type B				
HbO	8.0 ± 2.1	7.7 ± 2.1	**0,0012**	**-0,152**
HbR	7.1 ± 1.9	7.9 ± 1.9	**0,0007**	**0,425**
HbT	7.6 ± 2.3	8.1 ± 2.3	**0,0007**	**0,179**
H_2O	8.2 ± 2.2	8.0 ± 2.2	0,2121	-0,067
MREG	9.1 ± 3.0	9.5 ± 3.0	**0,0144**	**0,135**
Type C				
HbO	5.8 ± 1.5	6.0 ± 1.3	**0,0099**	**0,123**
HbR	5.7 ± 1.2	6.0 ± 1.3	**0,0007**	**0,198**
HbT	5.9 ± 1.5	6.0 ± 1.4	**0,0302**	**0,107**
H_2O	5.9 ± 1.5	6.1 ± 1.5	0,1830	0,070
MREG	6.0 ± 1.5	6.5 ± 1.6	**0,0007**	**0,183**
Type D				
HbO	5.8 ± 2.4	6.0 ± 2.1	**0,0043**	**0,079**
HbR	5.6 ± 1.7	5.9 ± 2.1	**0,0007**	**0,179**
HbT	6.0 ± 2.3	6.1 ± 2.3	0,0870	0,049
H_2O	6.0 ± 2.5	6.0 ± 2.3	0,6598	-0,015
MREG	6.8 ± 2.7	6.5 ± 3.0	**0,0026**	**-0,097**

Table 5. Calculated average (Mean) and standard deviation (SD) of diverse CBP types of AD patients and healthy controls on the basis of PRD of fNIRS and MREG data. One timepoint correspond to 0.1 second due to the sample rate of fNIRS and MREG. Bolded numbers are statistically significant results ($p < 0.05$).

FNIRS and MREG detected a significant difference in PRD of type A, where PRD was decreased in AD patients (HbR: 4.3 ± 0.9 vs 4.2 ± 1.2, $p < 0.01$, $d = -0.125$; MREG: 4.7 ± 1.5 vs 4.4 ± 1.6, $p < 0.001$, $d = -0.244$). Furthermore, fNIRS and MREG detected a significant difference in PRD of type B, where PRD was increased in AD patients (HbR: 7.1 ± 1.9 vs 7.9 ± 1.9, $p < 0.001$, $d = 0.425$; HbT: 7.6 ± 2.3 vs 8.1 ± 2.3, $p < 0.05$ $d = 0.179$; MREG: 9.1 ± 3.0 vs 9.5 ± 3.0, $p < 0.05$, $d = 0.135$). However, in HbO, the PRD was decreased in AD patients (HbO: 8.0 ± 2.1 vs 7.7 ± 2.1, $p < 0.01$, $d = -0.152$). Both methods detected increased PRD of type C in AD patients (HbO: 5.8 ± 1.5 vs 6.0 ± 1.3, $p < 0.01$, $d = 0.123$; HbR: 5.7 ± 1.2 vs 6.0 ± 1.3, $p < 0.001$, $d = 0.198$; HbT: 5.9 ± 1.5 vs 6.0 ± 1.4, $p < 0.05$, $d = 0.107$; MREG: 6.0 ± 1.5 vs 6.5 ± 1.6, $p < 0.001$, $d = 0.183$). FNIRS showed increased PRD of type D in AD patients (HbO: 5.8 ± 2.4 vs 6.0 ± 2.1, $p < 0.01$, $d = 0.079$; HbR: 5.6 ± 1.7 vs 5.9 ± 2.1, $p < 0.001$, $d = 0.179$). However, MREG detected decreased PRD of type D in AD patients (MREG: 6.8 ± 2.7 vs 6.5 ± 3.0, $p < 0.01$, $d = -0.097$). The PRD results were shown in **Table 5.** and **Fig 6-3**.

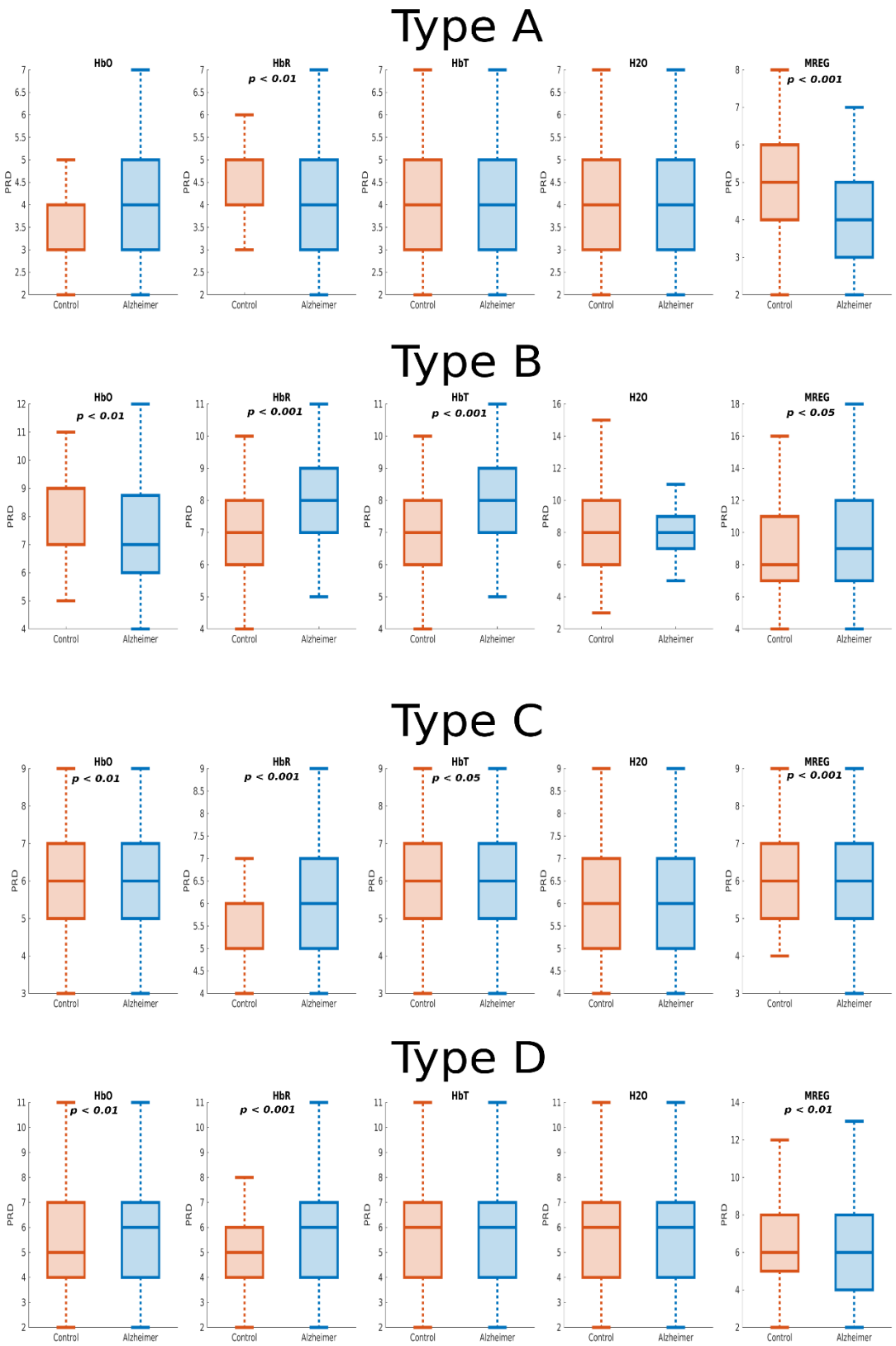

Figure 6-3. Boxplots of the properties of diverse CBP types of AD patients and healthy controls calculated on the basis of the PRD of fNIRS and MREG data. One timepoint correspond to 0.1 second due to the sample rate of fNIRS and MREG. The only statistically significant results is marked above the boxplot in question.

6.4 PFD

Mean ± SD	Control	Alzheimer		
Type A	PFD	PFD	P-values	Effect size
HbO	6.7 ± 2.1	6.9 ± 2.2	0,1318	0,074
HbR	6.4 ± 1.5	6.8 ± 1.9	**0,0007**	**0,204**
HbT	7.1 ± 2.4	6.7 ± 2.3	**0,0018**	**-0,154**
H_2O	7.0 ± 2.3	6.8 ± 2.2	0,1751	-0,067
MREG	7.7 ± 2.9	7.8 ± 3.0	0,7668	0,022
Type B				
HbO	3.1 ± 1.2	3.2 ± 1.2	0,1089	0,081
HbR	3.3 ± 1.0	3.1 ± 1.0	**0,0117**	**-0,115**
HbT	3.1 ± 1.2	3.3 ± 1.2	**0,0007**	**0,194**
H_2O	3.0 ± 1.2	3.2 ± 1.2	**0,0132**	**0,117**
MREG	3.6 ± 1.5	3.7 ± 1.5	0,5061	0,043
Type C				
HbO	4.9 ± 1.5	4.9 ± 1.4	0,6196	0,030
HbR	4.8 ± 1.2	5.0 ± 1.2	**0,0012**	**0,140**
HbT	4.8 ± 1.6	5.0 ± 1.4	**0,0144**	**0,121**
H_2O	5.0 ± 1.5	5.1 ± 1.4	0,2676	0,061
MREG	5.0 ± 1.5	5.4 ± 1.7	**0,0007**	**0,201**
Type D				
HbO	5.0 ± 2.2	5.0 ± 2.2	0,1342	-0,044
HbR	5.0 ± 1.8	5.0 ± 2.1	0,1651	0,039
HbT	4.9 ± 2.4	5.0 ± 2.1	0,2118	0,037
H_2O	5.1 ± 2.4	5.1 ± 2.2	0,7311	0,013
MREG	5.2 ± 2.5	5.8 ± 2.8	**0,0007**	**0,206**

Table 6. Calculated average (Mean) and standard deviation (SD) of diverse CBP types of AD patients and healthy controls on the basis of PFD of fNIRS and MREG data. One timepoint correspond to 0.1 second due to the sample rate of fNIRS and MREG. Bolded numbers are statistically significant results ($p < 0.05$).

FNIRS detected changes in the PFD of type A. PFD was increased in AD patients (HbR: 6.4 ± 1.5 vs 6.8 ± 1.9, $p < 0.001$, $d = 0.204$), but in HbT, PFD was decreased in AD patients (HbT: 7.1 ± 2.4 vs 6.7 ± 2.3, $p < 0.01$, $d = -0.154$). Furthermore, fNIRS detected changes in PFD of type B. PFD was increased in AD patients (HbT: 3.3 ± 1.0 vs 3.1 ± 1.0, $p < 0.001$, $d = 0.194$; H2O: 3.0 ± 1.2 vs 3.3 ± 1.2, $p < 0.05$, $d = 0.117$). However, in HbR, PFD was decreased in AD patients (HbR: 3.3 ± 1.0 vs 3.1 ± 1.0, $p < 0.05$, $d = -0.115$). FNIRS and MREG showed a significant difference in PFD of type C between AD patients and healthy controls, where PFD was increased in AD patients (HbR: 4.8 ± 1.2 vs 5.0 ± 1.2, $p < 0.01$, $d = 0.140$; HbT: 4.8 ± 1.6 vs 5.0 ± 1.4, $p < 0.05$, $d = 0.121$; MREG: 5.0 ± 1.5 vs 5.4 ± 1.7, $p < 0.001$, $d = 0.201$). MREG showed increased PFD of type D in AD patients (MREG: 5.2 ± 2.5 vs 5.8 ± 2.8, $p < 0.001$, $d = 0.206$). the PFD results were shown in **Table 6.** and **Fig 6-4**.

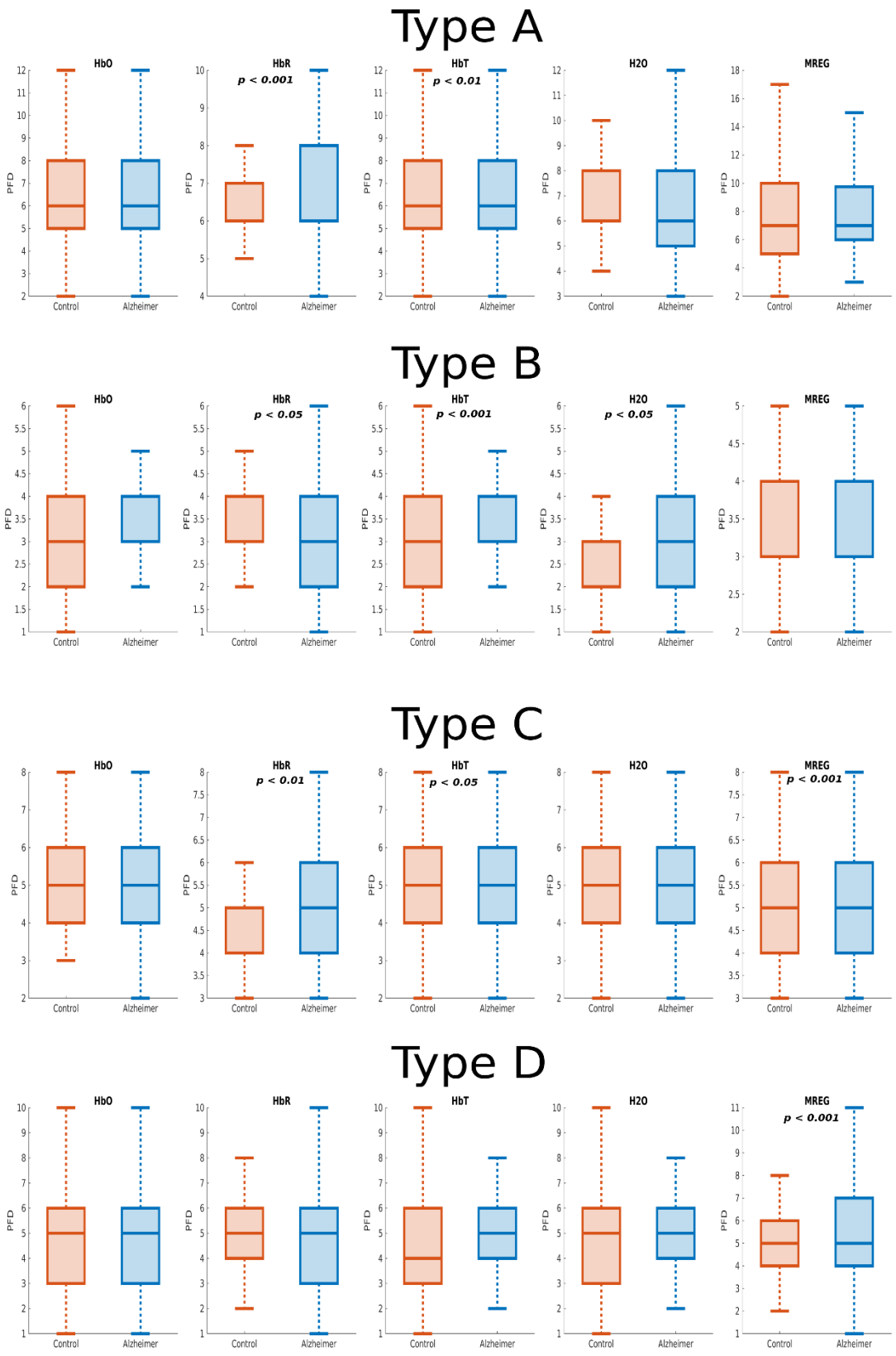

Figure 6-4. Boxplots of the properties of diverse CBP types of AD patients and healthy controls calculated on the basis of the PFD of fNIRS and MREG data. One timepoint correspond to 0.1 second due to the sample rate of fNIRS and MREG. The only statistically significant results is marked above the boxplot in question.

6.5 PA_1

Mean ± SD	Control	Alzheimer		
Type A	Pulse angle 1	Pulse angle 1	P-values	Effect size
HbO	64.7 ± 7.1	64.6 ± 7.2	0,6909	-0,024
HbR	62.3 ± 5.8	64.7 ± 7.2	**0,0007**	**0,363**
HbT	65.1 ± 7.3	64.2 ± 7.4	**0,0174**	**-0,115**
H_2O	64.8 ± 7.2	64.2 ± 7.2	0,0849	-0,083
MREG	63.7 ± 7.4	66.0 ± 8.0	**0,0007**	**0,308**
Type B				
HbO	24.8 ± 7.1	26.3 ± 7.1	**0,0007**	**0,203**
HbR	28.6 ± 7.0	25.2 ± 7.0	**0,0007**	**-0,518**
HbT	25.8 ± 7.2	25.9 ± 7.2	0,8456	0,013
H_2O	24.1 ± 7.3	24.8 ± 7.3	0,0625	0,093
MREG	24.9 ± 7.9	24.5 ± 7.9	0,2973	-0,064
Type C				
HbO	45.5 ± 5.2	44.7 ± 5.2	**0,0007**	**-0,172**
HbR	45.0 ± 5.5	45.0 ± 5.2	0,9867	-0,001
HbT	44.7 ± 5.3	45.0 ± 5.2	0,3090	0,056
H_2O	45.2 ± 5.1	45.3 ± 5.1	0,5177	0,038
MREG	45.2 ± 5.1	45.3 ± 5.3	0,7089	0,026
Type D				
HbO	46.7 ± 17.8	44.7 ± 16.7	**0,0007**	**-0,115**
HbR	46.7 ± 14.7	45.7 ± 17.6	**0,0198**	**-0,061**
HbT	43.9 ± 17.8	44.4 ± 16.9	0,2866	0,033
H_2O	45.4 ± 18.2	45.4 ± 17.3	0,7700	0,011
MREG	42.7 ± 16.5	46.9 ± 18.4	**0,0007**	**0,239**

Table 7. Calculated average (Mean) and standard deviation (SD) of diverse CBP types of AD patients and healthy controls on the basis of PA_1 of fNIRS and MREG data. Bolded numbers are statistically significant results ($p < 0.05$).

FNIRS and MREG showed a significant difference in PA_1 of type A between AD patients and healthy controls, where PA_1 was increased in AD patients (HbR: 62.3 ± 5.8 vs 65.1 ± 7.3, $p < 0.001$, $d = 0.363$; MREG: 63.7 ± 7.4 vs 66.0 ± 8.0, $p < 0.001$, $d = 0.308$). However, in HbT, PA_1 was decreased in AD patients (HbT: 65.1 ± 7.3 vs 64.2 ± 7.4, $p < 0.05$, $d = -0.115$). FNIRS detected a significant difference in PA_1 of type B, where PA_1 was increased in AD patients (HbO: 24.8 ± 7.1 vs 26.3 ± 7.1 in AD, $p < 0.001$, $d = 0.203$). However, in HbR, PA_1 was decreased in AD patients (HbR: 28.6 ± 7.0 vs 25.2 ± 7.0, $p < 0.001$, $d = -0.518$). Furthermore, fNIRS detected a significant difference in PA_1 of type C between AD patients and healthy controls, where PA_1 was decreased in AD patients (HbO: 45.5 ± 5.2 vs 44.7 ± 5.2, $p < 0.001$, $d = 0.172$). Both methods showed a significant difference in PA_1 of type D. PA_1 of HbO and HbR were decreased in AD patients (HbO: 46.7 ± 17.8 vs 44.7 ± 16.7, $p < 0.001$, $d = -0.115$; HbR: 46.7 ± 14.7 vs 45.7 ± 17.6, $p < 0.05$, $d = -0.061$). However, PA_1 of MREG was increased in AD patients (MREG: 42.7 ± 16.5 vs 46.9 ± 18.4, $p < 0.001$, $d = -0.239$). The PA_1 results were shown in **Table 7.** and **Fig 6-5**.

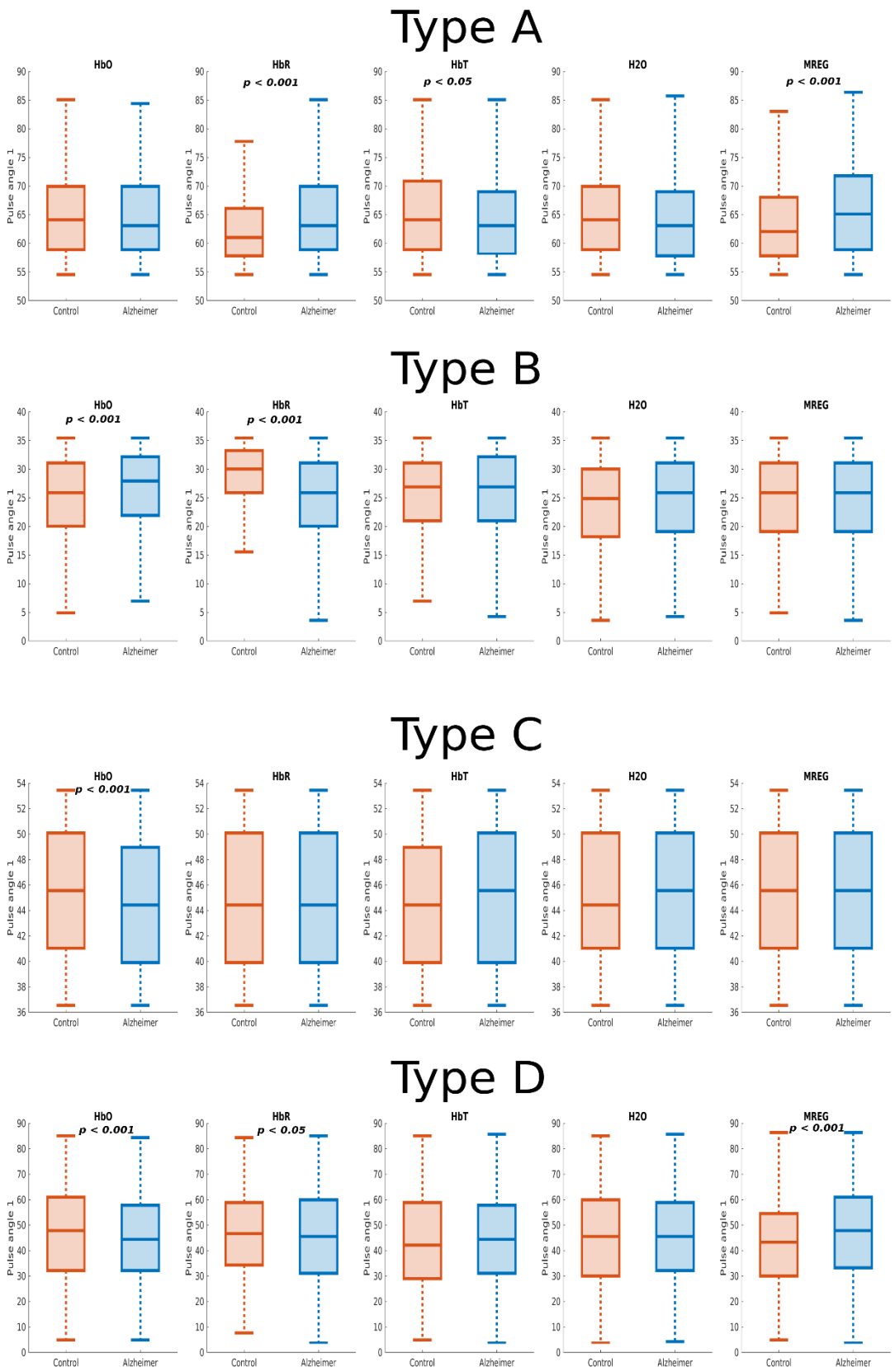

Figure 6-5. Boxplots of the properties of diverse CBP types of AD patients and healthy controls calculated on the basis of the PA_1 of fNIRS and MREG data. The only statistically significant results is marked above the boxplot in question.

6.6 PA_2

Mean ± SD	Control	Alzheimer		
Type A	Pulse angle 2	Pulse angle 2	P-values	Effect size
HbO	25.3 ± 7.1	25.4 ± 7.2	0,6977	0,024
HbR	27.7 ± 5.8	25.3 ± 7.2	**0,0007**	**-0,363**
HbT	24.9 ± 7.3	25.8 ± 7.4	**0,0154**	**0,115**
H_2O	25.3 ± 7.2	25.8 ± 7.2	0,0844	0,083
MREG	26.3 ± 7.4	24.0 ± 8.0	**0,0007**	**-0,308**
Type B				
HbO	65.2 ± 7.1	63.7 ± 7.1	**0,0007**	**-0,203**
HbR	61.4 ± 7.0	64.8 ± 7.0	**0,0007**	**0,518**
HbT	64.2 ± 7.2	64.1 ± 7.2	0,8469	-0,013
H_2O	65.9 ± 7.3	65.2 ± 7.3	0,0618	-0,093
MREG	65.1 ± 7.9	65.5 ± 7.9	0,2987	0,064
Type C				
HbO	44.5 ± 5.2	45.3 ± 5.2	**0,0012**	**0,172**
HbR	45.0 ± 5.5	45.0 ± 5.2	0,9867	0,001
HbT	45.3 ± 5.3	45.0 ± 5.2	0,3176	-0,056
H_2O	44.8 ± 5.1	44.7 ± 5.1	0,5177	-0,038
MREG	44.8 ± 5.1	44.7 ± 5.3	0,7075	-0,026
Type D				
HbO	43.3 ± 17.8	45.3 ± 16.7	**0,0007**	**0,115**
HbR	43.3 ± 14.7	44.3 ± 17.6	**0,0177**	**0,061**
HbT	46.1 ± 17.8	45.6 ± 16.9	0,2703	-0,033
H_2O	44.6 ± 18.2	44.4 ± 17.3	0,7668	-0,011
MREG	47.3 ± 16.5	43.1 ± 18.4	**0,0007**	**-0,239**

Table 8. Calculated average (Mean) and standard deviation (SD) of diverse CBP types of AD patients and healthy controls on the basis of PA_2 of fNIRS and MREG data. Bolded numbers are statistically significant results ($p < 0.05$).

Both methods provided a significant difference in PA_2 of type A between AD patients and healthy controls, where PA_2 was decreased in AD patients (HbR: 27.7 ± 5.8 vs 25.3 ± 7.2, $p < 0.001$, $d = -0.363$; MREG: 26.3 ± 7.4 vs 24.0 ± 8.0, $p < 0.001$, $d = -0.308$). However, in HbT, PA_2 was increased in AD patients (HbT: 24.9 ± 7.3 vs 25.8 ± 7.4, $p < 0.05$, $d = 0.115$). FNIRS detected changes in PA_2 of type B, where PA_2 of HbO was decreased in AD patients (HbO: 65.2 ± 7.1 vs 63.7 ± 7.1, $p < 0.001$, $d = -0.203$). However, PA_2 of HbR was increased in AD patients (HbR: 61.4 ± 7.0 vs 64.8 ± 7.0, $p < 0.001$, $d = 0.518$). Furthermore, fNIRS detected changes in PA_2 of type C, where PA_2 was increased in AD patients (HbO: 44.5 ± 5.2 vs 45.3 ± 5.2, $p < 0.001$, $d = 0.172$). Both methods detected a significant difference in PA_2 of type D. PA_2 of HbO and HbR were increased in AD patients (HbO: 43.3 ± 17.8 vs 45.3 ± 16.7, $p < 0.001$, $d = 0.115$; HbR: 43.3 ± 14.7 vs 44.3 ± 17.6, $p < 0.05$, $d = 0.061$). However, in MREG, PA_2 was decreased in AD patients (MREG: 47.3 ± 16.5 vs 43.1 ± 18.4, $p < 0.001$, $d = -0.239$). The PA_2 results were shown in **Table 8.** and **Fig 6-6**.

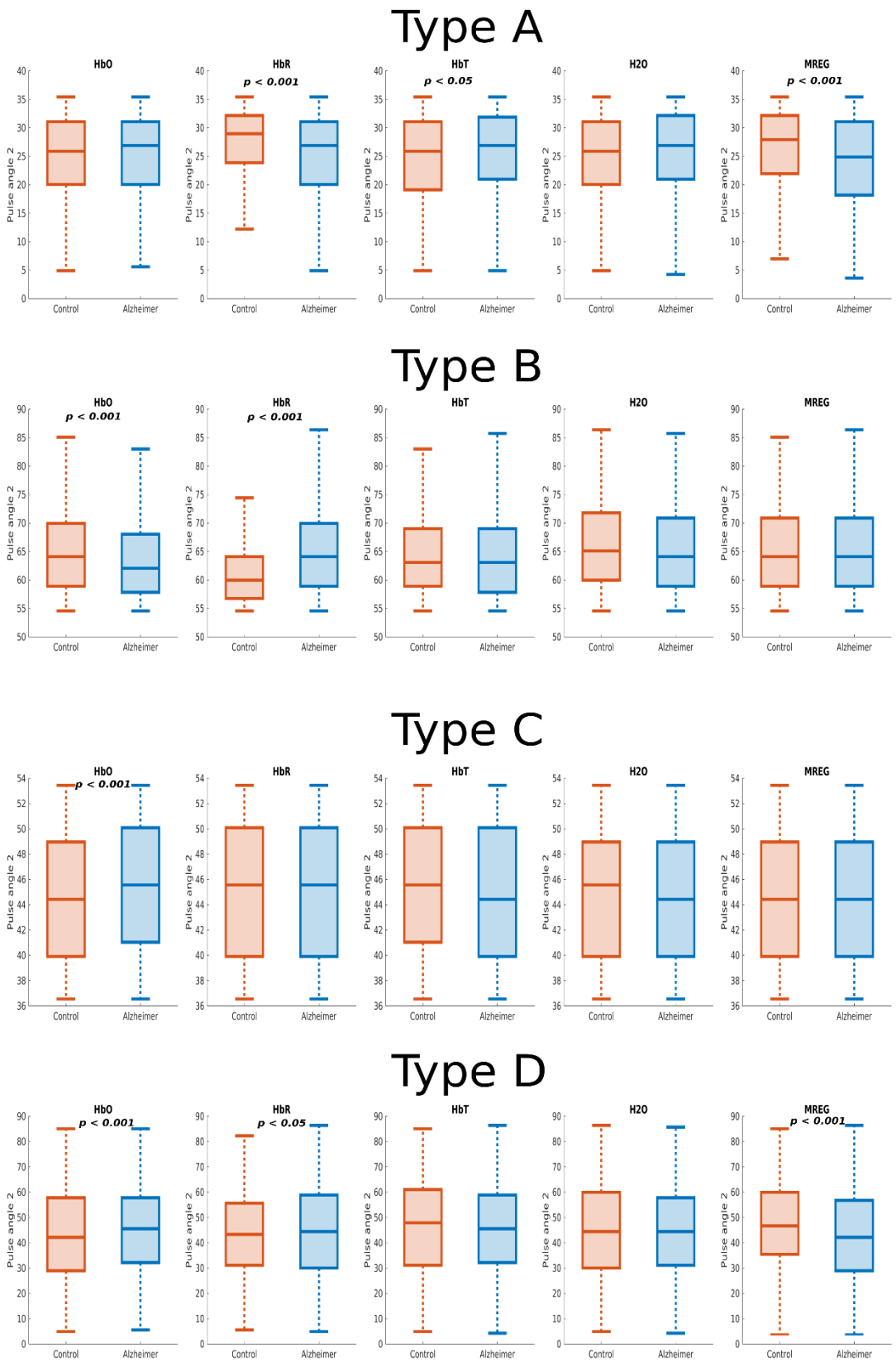

Figure 6-6. Boxplots of the properties of diverse CBP types of AD patients and healthy controls calculated on the basis of the PA_2 of fNIRS and MREG data. The only statistically significant results is marked above the boxplot in question.

7 DISCUSSION

Multiple studies indicate changes in cardiovascular brain pulsations of AD patients [80]–[86]. Furthermore, in-depth analysis within the target MREG brain averaged region-of-interest signal under the fNIRS frontal probing area, the CBP parameters in MREG and fNIRS showed significant changes in AD patients within each CBP type. Therefore, fNIRS can identify different brain fluid compartments, which can be cross-verified with MREG.

The overall pulse amount (cf. **Table 2.**) when compared between MREG and fNIRS was slightly lower in MREG compared to fNIRS in each CBP type. This factor seems to indicate that fNIRS was more sensitive to detecting CBP when compared to MREG. MREG being less sensitive to detecting CBP might be associated with its signal variability, where signal variability of AD patients was increased when compared to healthy controls in the cardiac frequency band [24]. On the contrary, unsuitable pulses might be detected in fNIRS signals because of being more sensitive. The solution for measuring the sensitivity of detecting CBP is to apply blood pressure measurements during fNIRS and MREG imaging. Therefore, blood pressure measurements offer a comprehensive overall pulse amount, which can be compared to the overall pulse amount of fNIRS and MREG.

There were a few exceptions in the overall pulse amount. The overall pulse amount in AD patients was lower in MREG than in fNIRS within type A. Although calculating the type A pulse amount showed a significant difference in MREG, the pulse amount was increased in AD patients. However, the overall pulse amount in AD patients was increased as well in MREG signals within type D. In conclusion, overall pulse amounts between AD patients and healthy controls were close to each other, which reflected stability pulse detection in AD patients and healthy controls.

The alterations in PD of type A pulse were presented in fNIRS, where PD of arterial HbO and venous HbR in the AD patients was more prolonged than healthy controls. These results could indicate altered arterial pulsation in AD patients by the effect of altered cerebral blood flow. However, in HbT, the PD was shorter in AD patients than in healthy controls. MREG, venous HbR, and HbT detected alterations in PD of type B where the PD of AD patients was longer when compared to healthy controls. These findings imply that the altered venous pulsation observed in AD patients may be attributed to alterations in the deoxygenated blood flow. The alterations in PD of types C and D were similar to the alterations in PD of type B, where PD of AD patients was longer when compared to healthy controls.

PRD changes were detected in MREG and fNIRS data within each CBP type. In type A, PRD changes were detected in venous HbR and MREG, where the PRD of AD patients was more prolonged than that of healthy controls. The PRD of type B were detected in MREG, venous HbR, and HbT, where the PRD of AD patients were longer when compared to healthy controls. These findings suggest that the effects of altered deoxygenated blood flow in AD patients cause an alteration in venous pulsation during the systolic phase. However, in arterial HbO, the PRD of type B was shorter in AD patients than in healthy controls. The alterations in PRD of type C were shown

in MREG, arterial HbO, venous HbR, and HbT, where the PRD of AD patients was longer when compared to healthy controls. The alterations in PRD of type D were similar to PRD of type C, except that HbT did not show a significant difference in PRD.

PFD changes were detected in each CBP type with both imaging methods. In type A, PFD changes were seen in venous HbR and HbT. PFD of AD patients was longer when compared to healthy controls in venous HbR. However, in HbT, the PFD of AD patients was shorter than that of healthy controls. This result seems to indicate alterations in cerebral blood flow during arterial pulsation during the diastolic phase in AD patients. Furthermore, fNIRS detected changes in PFD of type B, where, in HbR, the PFD of AD patients was longer when compared to healthy controls. However, in HbT and H_2O, the PFD of AD patients was shorter than that of healthy controls. These results imply the altered cerebral blood and water flow in the venous pulsation during the diastolic phase of AD patients. The alterations in PFD of type C were seen in venous HbR, HbT and MREG, where the PFD of AD patients was longer when compared to healthy controls. MREG detected changes in PFD of type D, where the PFD of AD patients was more extended than that of healthy controls.

The PA_1 results are similar to the PA_2 results because of being the opposite angle by assuming the pulse shape being a rectangular triangle. Hence, the statistical analysis as well provides a similar result with opposite effect sizes since the distribution of the population of PA_1 and PA_2 of AD patients and healthy controls have similar values both in fNIRS and MREG. Although, changes in the PA_1 and PA_2 appeared mostly in fNIRS.

PA_1 and PA_2 of type A alterations were detected in MREG and venous HbR, where PA_1 of AD patients was narrower when compared to healthy controls, and PA_2 of AD patients was broader than that of healthy controls. However, in HbT of type A, the PA_1 of AD patients was narrower when compared to healthy controls, and the PA_2 of AD patients was broader when compared to healthy controls. Therefore, the result seems to indicate the alterations in cerebral blood flow affects the shape of arterial pulsation in AD patients. FNIRS detected changes in PA_1 and PA_2 of type B. In arterial HbO, the PA_1 of AD patients was wider when compared to healthy controls, and in venous HbR, the PA_1 of AD patients was narrower than that of healthy controls. In arterial HbO, the PA_2 of AD patients was narrower when compared to healthy controls, and in venous HbR, the PA_2 of AD patients were broader when compared to healthy controls. These results suggest that altered cerebral blood flow affects the shape of venous pulsation in AD patients. The alterations in PA_1 and PA_2 of type C were seen in arterial HbO, where PA_1 of AD patients was narrower when compared to healthy controls, and PA_2 of AD patients was broader than that of healthy controls. MREG and fNIRS detected changes in PA_1 and PA_2 of type D. In MREG, PA_1 of AD patients was wider when compared to healthy controls, but in arterial HbO and venous HbR, PA_1 of AD patients was narrower than that of healthy controls. In MREG, the PA_2 of AD patients were narrower than that of healthy controls, but in arterial HbO and venous HbR, the PA_2 of AD patients was wider when compared to healthy controls.

The results may be connected to the effect of impaired cerebral autoregulation in AD [87]–[89]. Cerebral autoregulation is based on maintaining the blood flow within a specific blood pressure range [90]. Multiple studies show a correlation between blood flow and blood pressure [87], [90], [91], where impaired cerebral autoregulation is associated with altered blood pressure. Hence, altered blood pressure would influence cerebral blood flow. Increased blood pressure is associated

with arterial stiffness by changing the structure of blood vessels [13], [17], [92], [93], which may be detected in the results of arterial HbO and MREG within type A.

However, decreased blood pressure with brain hypoperfusion is linked to brain atrophy [94]. In addition, altered deoxygenated blood flow may be linked to brain atrophy, which might be detected in the results of venous HbR and MREG within types B and C. Increased cerebral venous and intracranial pressure from jugular compression affects venous overflow, which limits the cranial space for arterial expansion and increases the expulsion of CSF from the ventricles [95]. Hence, disordered venous drainage and dysfunctional BBB at venules in perivascular channels, caused by CSF overflow due to venous hypertension, alter the structural properties of the veins [96]–[98]. This was possibly seen in the results of venous, HbR and MREG within types B and C as well. Decreased cerebral blood flow and cerebral blood volume constricts capillaries in AD [99], [100] by decreasing the removal of amyloid accumulation, which could be seen in the results of venous HbR and MREG within types B and C. Furthermore, multiple studies indicated an alteration in cerebral blood flow velocity during AD [74], [80], [89], [101], which is also associated with impaired cerebral autoregulation. In addition, changes in blood pressure, blood flow rate and velocity during AD might cause changes in blood volume. Hence, changes in blood volume might be detected in diverse CBP types.

AQP4 depolarisation causes decreasing efficiency of the glymphatic clearance system. It increases amyloid accumulation in AD [21], [102], where altered arterial pulsation might be seen in the results of MREG, arterial HbO and HbT within type A. Furthermore, venous outflow pathway impairs the glymphatic clearance system due to CSF overflow [95]–[97], [103]. However, the glymphatic outflow system could have a compensatory mechanism by maintaining the intracranial pressure [103]. Impaired CSF drainage by venous flow could still alter the structures of venules even though changes in intracranial pressure are not detected [103]. Therefore, venous, HbR, and MREG results within types B and C are capable to show venule alteration, which is associated with an impaired glymphatic system.

8 CONCLUSION

This study provides novel findings about the cardiovascular system in the brain by calculating the CBP parameters. Therefore, type A, B, and C pulses seem to represent a function of arterial, venous and tissue pulses. FNIRS brain fluid compartments are distinguishable from the diverse CBP types because of measuring brain fluid activity. Most of the results from MREG and fNIRS cross-verify each other. Hence, implying that a relation between MREG and the brain fluid compartments is detectable. Alterations of cardiovascular brain pulsation in AD are primarily detected in brain blood fluid compartments within both methods.

The connection between an impaired glymphatic system and altered cerebral autoregulation could be detected in the results of MREG and fNIRS. The impaired glymphatic system is associated with not only artery hypertension but also venous hypertension. Therefore, conducting more studies to show a connection between the glymphatic system and cerebral autoregulation in AD could be beneficial for developing an early detection method for AD. In addition, studying the relationship between AD and venous hypertension seems to be essential to understand the connection between the glymphatic system and cerebral autoregulation in AD.

Developing the algorithm for measuring the CBP parameters could lead to detectable findings about cerebral autoregulation and the glymphatic system because of detecting structural changes in CBP. However, the CBP parameters combined with blood pressure and blood flow velocity could give profound knowledge about cerebral autoregulation and the glymphatic system because of receiving more comprehensive details about brain hemodynamics. Furthermore, conducting more studies about CBP in neurodegenerating diseases may demonstrate the advantages of detecting alteration in CBP at brain blood vessels.

The combination of fNIRS and MREG could lead us to discover the latest information about AD and the development of promising diagnostic devices to measure the development of AD. The benefit of using fNIRS and MREG is combining high temporal resolution of fNIRS with high spatial resolution of MREG to gain detailed cerebral hemodynamic findings of the cortex. Therefore, combining MREG and fNIRS may be an efficient biomarker of AD by detecting hemodynamic changes in the brain. In addition, combining MREG and fNIRS validates the results of fNIRS. However, fNIRS to measure CBP have some advantages when compared to MREG. FNIRS is a cheap, fast and non-invasive imaging method with more comprehensive usability. In contrast to MREG, fNIRS can distinguish brain fluid into its compartments by measuring their wavelengths from light. Unfortunately, fNIRS have a limited spatial resolution due to its light penetration depth. Nonetheless, fNIRS could be a preliminary biomarker of AD by reflecting structural changes in a cardiac pulse within brain fluid compartments while measuring CBP parameters.

9 REFERENCES

[1] R. van der Kant, L. S. B. Goldstein, and R. Ossenkoppele, 'Amyloid-β-independent regulators of tau pathology in Alzheimer disease', *Nat Rev Neurosci*, vol. 21, no. 1, pp. 21–35, 2020, doi: 10.1038/s41583-019-0240-3.

[2] D. J. Selkoe, 'The molecular pathology of Alzheimer's disease', *Neuron*, vol. 6, no. 4, pp. 487–498, 1991, doi: https://doi.org/10.1016/0896-6273(91)90052-2.

[3] J. L. Cummings, 'Alzheimer's Disease', *New England Journal of Medicine*, vol. 351, no. 1, pp. 56–67, Jul. 2004, doi: 10.1056/NEJMra040223.

[4] D. J. Selkoe and J. Hardy, 'The amyloid hypothesis of Alzheimer's disease at 25 years', *EMBO Mol Med*, vol. 8, no. 6, pp. 595–608, Jun. 2016, doi: 10.15252/emmm.201606210.

[5] D. S. Knopman, 'Lowering of Amyloid-Beta by β-Secretase Inhibitors — Some Informative Failures', *New England Journal of Medicine*, vol. 380, no. 15, pp. 1476–1478, Apr. 2019, doi: 10.1056/NEJMe1903193.

[6] E. S. Musiek and D. M. Holtzman, 'Three dimensions of the amyloid hypothesis: time, space and "wingmen"', *Nat Neurosci*, vol. 18, no. 6, pp. 800–806, 2015, doi: 10.1038/nn.4018.

[7] Nanfei Sun, M. Garbey, A. Merla, and I. Pavlidis, 'Imaging the Cardiovascular Pulse', in *2005 IEEE Computer Society Conference on Computer Vision and Pattern Recognition (CVPR'05)*, IEEE, pp. 416–421. doi: 10.1109/CVPR.2005.184.

[8] K. Yaffe, 'Prevention of Cognitive Impairment With Intensive Systolic Blood Pressure Control', *JAMA*, vol. 321, no. 6, pp. 548–549, Feb. 2019, doi: 10.1001/jama.2019.0008.

[9] S. M. I. for the S. R. Group *et al.*, 'Effect of Intensive vs Standard Blood Pressure Control on Probable Dementia: A Randomized Clinical Trial', *JAMA*, vol. 321, no. 6, pp. 553–561, Feb. 2019, doi: 10.1001/jama.2018.21442.

[10] M. Kivipelto *et al.*, 'Midlife vascular risk factors and late-life mild cognitive impairment', *Neurology*, vol. 56, no. 12, p. 1683, Jun. 2001, doi: 10.1212/WNL.56.12.1683.

[11] J. G. Abell *et al.*, 'Association between systolic blood pressure and dementia in the Whitehall II cohort study: role of age, duration, and threshold used to define hypertension', *Eur Heart J*, vol. 39, no. 33, pp. 3119–3125, Sep. 2018, doi: 10.1093/eurheartj/ehy288.

[12] J. M. Gabin, K. Tambs, I. Saltvedt, E. Sund, and J. Holmen, 'Association between blood pressure and Alzheimer disease measured up to 27 years prior to diagnosis: the HUNT Study', *Alzheimers Res Ther*, vol. 9, no. 1, p. 37, 2017, doi: 10.1186/s13195-017-0262-x.

[13] C. Qiu, B. Winblad, and L. Fratiglioni, 'The age-dependent relation of blood pressure to cognitive function and dementia', *Lancet Neurol*, vol. 4, no. 8, pp. 487–499, 2005, doi: https://doi.org/10.1016/S1474-4422(05)70141-1.

[14] J. B. S. Langbaum *et al.*, 'Blood pressure is associated with higher brain amyloid burden and lower glucose metabolism in healthy late middle-age persons', *Neurobiol Aging*, vol. 33, no. 4, pp. 827.e11-827.e8.27E19, Apr. 2012, doi: 10.1016/j.neurobiolaging.2011.06.020.

[15] E. S. C. Korf, L. R. White, P. Scheltens, and L. J. Launer, 'Midlife blood pressure and the risk of hippocampal atrophy: the Honolulu Asia Aging Study.', *Hypertension*, vol. 44, no. 1, pp. 29–34, Jul. 2004, doi: 10.1161/01.HYP.0000132475.32317.bb.

[16] D. H. Bergel, 'The dynamic elastic properties of the arterial wall', *J Physiol*, vol. 156, no. 3, pp. 458–469, May 1961, doi: https://doi.org/10.1113/jphysiol.1961.sp006687.

[17] M. E. Safar, B. I. Levy, and H. Struijker-Boudier, 'Current Perspectives on Arterial Stiffness and Pulse Pressure in Hypertension and Cardiovascular Diseases', *Circulation*, vol. 107, no. 22, pp. 2864–2869, Jun. 2003, doi: 10.1161/01.CIR.0000069826.36125.B4.

[18] M. E. Safar, O. Henry, and S. Meaume, 'Aortic Pulse Wave Velocity: An Independent Marker of Cardiovascular Risk', *Am J Geriatr Cardiol*, vol. 11, no. 5, pp. 295–304, Jun. 2007, doi: 10.1111/j.1076-7460.2002.00695.x.

[19] A. D. Stewart, B. Jiang, S. C. Millasseau, J. M. Ritter, and P. J. Chowienczyk, 'Acute reduction of blood pressure by nitroglycerin does not normalize large artery stiffness in essential hypertension.', *Hypertension*, vol. 48, no. 3, pp. 404–10, Sep. 2006, doi: 10.1161/01.HYP.0000237669.64066.c5.

[20] M. Kivipelto *et al.*, 'The Finnish Geriatric Intervention Study to Prevent Cognitive Impairment and Disability (FINGER): Study design and progress', *Alzheimer's and Dementia*, vol. 9, no. 6, 2013, doi: 10.1016/j.jalz.2012.09.012.

[21] N. Jessen, A. Munk, I. Lundgaard, and M. Nedergaard, 'The Glymphatic System: A Beginner's Guide', *Neurochem Res*, vol. 40, no. 12, pp. 2583–2599, Dec. 2015, doi: 10.1007/s11064-015-1581-6.

[22] H. Benveniste, X. Liu, S. Koundal, S. Sanggaard, H. Lee, and J. Wardlaw, 'The Glymphatic System and Waste Clearance with Brain Aging: A Review', *Gerontology*, vol. 65, no. 2, pp. 106–119, 2019, doi: 10.1159/000490349.

[23] V. Kiviniemi *et al.*, 'Ultra-fast magnetic resonance encephalography of physiological brain activity – Glymphatic pulsation mechanisms?', *Journal of Cerebral Blood Flow & Metabolism*, vol. 36, no. 6, pp. 1033–1045, Jun. 2016, doi: 10.1177/0271678X15622047.

[24] T. Tuovinen *et al.*, 'The variability of functional MRI brain signal increases in Alzheimer's disease at cardiorespiratory frequencies', *Sci Rep*, vol. 10, no. 1, p. 21559, 2020, doi: 10.1038/s41598-020-77984-1.

[25] B. C. Reeves *et al.*, 'Glymphatic System Impairment in Alzheimer's Disease and Idiopathic Normal Pressure Hydrocephalus', *Trends Mol Med*, vol. 26, no. 3, pp. 285–295, 2020, doi: https://doi.org/10.1016/j.molmed.2019.11.008.

[26] M. Järvelä, J. Kananen, V. Korhonen, N. Huotari, H. Ansakorpi, and V. Kiviniemi, 'Increased very low frequency pulsations and decreased cardiorespiratory pulsations suggest altered brain clearance in narcolepsy', *Communications Medicine*, vol. 2, no. 1, p. 122, Sep. 2022, doi: 10.1038/s43856-022-00187-4.

[27] P. K. Eide and G. Ringstad, 'Delayed clearance of cerebrospinal fluid tracer from entorhinal cortex in idiopathic normal pressure hydrocephalus: A glymphatic magnetic resonance imaging study', *Journal of cerebral blood flow and metabolism*, vol. 39, no. 7, pp. 1355–1368, Jul. 2019, doi: 10.1177/0271678X18760974.

[28] J. Kananen *et al.*, 'Altered physiological brain variation in drug-resistant epilepsy', *Brain Behav*, vol. 8, no. 9, p. e01090, Sep. 2018, doi: 10.1002/brb3.1090.

[29] J. Kananen *et al.*, 'Respiratory-related brain pulsations are increased in epilepsy—a two-centre functional MRI study', *Brain Commun*, vol. 2, no. 2, p. fcaa076, 2020, doi: 10.1093/braincomms/fcaa076.

[30] M. R and L. W, 'Sleep Facilitates Clearance of Metabolites from the Brain: Glymphatic Function in Aging and Neurodegenerative Diseases', *Rejuvenation Res*, 2013, doi: 10.1089/rej.2013.1530.

[31] L. Raitamaa *et al.*, 'Spectral analysis of physiological brain pulsations affecting the BOLD signal', *Hum Brain Mapp*, vol. 42, no. 13, 2021, doi: 10.1002/hbm.25547.

[32] V. Borchardt, V. Korhonen, H. Helakari, M. Nedergaard, T. Myllylä, and V. Kiviniemi, 'Inverse correlation of fluctuations of cerebral blood and water concentrations in humans', *Eur Phys J Plus*, vol. 136, no. 5, May 2021, doi: 10.1140/epjp/s13360-021-01480-2.

[33] T. Myllylä, M. Harju, V. Korhonen, A. Bykov, V. Kiviniemi, and I. Meglinski, 'Assessment of the dynamics of human glymphatic system by near-infrared spectroscopy', *J Biophotonics*, vol. 11, no. 8, pp. e201700123-n/a, Aug. 2018, doi: 10.1002/jbio.201700123.

[34] V. O. Korhonen *et al.*, 'Light Propagation in NIR Spectroscopy of the Human Brain', *IEEE journal of selected topics in quantum electronics*, vol. 20, no. 2, pp. 289–298, Mar. 2014, doi: 10.1109/JSTQE.2013.2279313.

[35] L. G. Apostolova, 'Alzheimer Disease', *CONTINUUM: Lifelong Learning in Neurology*, vol. 22, no. 2, Dementia, pp. 419–434, Apr. 2016, doi: 10.1212/CON.0000000000000307.

[36] J. L. Cummings, 'Alzheimer Disease', *JAMA*, vol. 287, no. 18, p. 2335, May 2002, doi: 10.1001/jama.287.18.2335.

[37] C. Duyckaerts, B. Delatour, and M.-C. Potier, 'Classification and basic pathology of Alzheimer disease', *Acta Neuropathol*, vol. 118, no. 1, pp. 5–36, 2009, doi: 10.1007/s00401-009-0532-1.

[38] Y.-J. Wang, H.-D. Zhou, and X.-F. Zhou, 'Clearance of amyloid-beta in Alzheimer's disease: progress, problems and perspectives', *Drug Discov Today*, vol. 11, no. 19–20, pp. 931–938, Oct. 2006, doi: 10.1016/j.drudis.2006.08.004.

[39] M. Goedert, 'Chapter 21 Neurofibrillary pathology of Alzheimer's disease and other tauopathies', 1998, pp. 287–306. doi: 10.1016/S0079-6123(08)64022-4.

[40] R. J. Castellani, R. K. Rolston, and M. A. Smith, 'Alzheimer Disease', *Disease-a-Month*, vol. 56, no. 9, pp. 484–546, Sep. 2010, doi: 10.1016/j.disamonth.2010.06.001.

[41] L. Kocsis, P. Herman, and A. Eke, 'The modified Beer–Lambert law revisited', *Phys Med Biol*, vol. 51, no. 5, pp. N91–N98, 2006, doi: 10.1088/0031-9155/51/5/N02.

[42] F. Scholkmann *et al.*, 'A review on continuous wave functional near-infrared spectroscopy and imaging instrumentation and methodology', *NeuroImage*, vol. 85. pp. 6–27, 2014. doi: //doi.org/10.1016/j.neuroimage.2013.05.004.

[43] J. T. Edsall, 'Blood and Hemoglobin: The Evolution of Knowledge of Functional Adaptation in a Biochemical System. Part I: The Adaptation of Chemical Structure to Function in Hemoglobin', *J Hist Biol*, vol. 5, no. 2, pp. 205–257, 1972, doi: 10.1007/BF00346659.

[44] K. von Vierordt 1818-1884, *Die quantitative spectralanalyse in ihrer Anwendung auf Physiologie, Physik, Chemie und Technologie*. Germany: H. Laupp, 1876, 1876. [Online]. Available: https://hdl.handle.net/2027/njp.32101074767862

[45] F. F. Jobsis, 'Noninvasive, infrared monitoring of cerebral and myocardial oxygen sufficiency and circulatory parameters', *Science (1979)*, vol. 198, no. 4323, pp. 1264–1267, 1977, doi: 10.1126/science.929199.

[46] M. Ferrari and V. Quaresima, 'A brief review on the history of human functional near-infrared spectroscopy (fNIRS) development and fields of application', *Neuroimage*, vol. 63, no. 2, pp. 921–935, 2012, doi: 10.1016/j.neuroimage.2012.03.049.

[47] A. Villringer and H. Obrig, 'Near-Infrared Spectroscopy and Imaging', in *Brain Mapping: The Methods*, Elsevier, 2002, pp. 141–158. doi: 10.1016/B978-012693019-1/50008-3.

[48] F. Amyot *et al.*, 'Assessment of cerebrovascular dysfunction after traumatic brain injury with fMRI and fNIRS', *Neuroimage Clin*, vol. 25, p. 102086, 2020, doi: 10.1016/j.nicl.2019.102086.

[49] P. Pouliot *et al.*, 'Nonlinear hemodynamic responses in human epilepsy: A multimodal analysis with fNIRS-EEG and fMRI-EEG', *J Neurosci Methods*, vol. 204, no. 2, pp. 326–340, Mar. 2012, doi: 10.1016/j.jneumeth.2011.11.016.

[50] F. Wallois, A. Patil, C. Héberlé, and R. Grebe, 'EEG-NIRS in epilepsy in children and neonates', *Neurophysiologie Clinique/Clinical Neurophysiology*, vol. 40, no. 5–6, pp. 281–292, Nov. 2010, doi: 10.1016/j.neucli.2010.08.004.

[51] V. R. Kondepati, H. M. Heise, and J. Backhaus, 'Recent applications of near-infrared spectroscopy in cancer diagnosis and therapy', *Anal Bioanal Chem*, vol. 390, no. 1, pp. 125–139, Jan. 2008, doi: 10.1007/s00216-007-1651-y.

[52] T. Myllylä, P. Karthikeyan, U. Honka, V. Korhonen, S. S. Karhula, and J. Nikkinen, 'Cerebral haemodynamic effects in the human brain during radiation therapy for brain cancer', in *Tissue Optics and Photonics*, Z. Zalevsky, V. v. Tuchin, and W. C. Blondel, Eds., SPIE, Apr. 2020, p. 76. doi: 10.1117/12.2555892.

[53] M. K. Yeung and J. Lin, 'Probing depression, schizophrenia, and other psychiatric disorders using fNIRS and the verbal fluency test: A systematic review and meta-analysis', *J Psychiatr Res*, vol. 140, pp. 416–435, Aug. 2021, doi: 10.1016/j.jpsychires.2021.06.015.

[54] D. Perpetuini, R. Bucco, M. Zito, and A. Merla, 'Study of memory deficit in Alzheimer's disease by means of complexity analysis of fNIRS signal', *Neurophotonics (Print)*, vol. 5, no. 1, p. 011010, 2018, doi: 10.1117/1.NPh.5.1.011010.

[55] D. Perpetuini *et al.*, 'Complexity of Frontal Cortex fNIRS Can Support Alzheimer Disease Diagnosis in Memory and Visuo-Spatial Tests', *Entropy (Basel)*, vol. 21, no. 1, p. 26, 2019, doi: 10.3390/e21010026.

[56] A. H. E. A. van Beek, J. Lagro, M. G. M. Olde-Rikkert, R. Zhang, and J. A. H. R. Claassen, 'Oscillations in cerebral blood flow and cortical oxygenation in Alzheimer's disease', *Neurobiol Aging*, vol. 33, no. 2, pp. 428.e21-428.e31, 2012, doi: 10.1016/j.neurobiolaging.2010.11.016.

[57] J. B. M. Zeller, M. J. Herrmann, A.-C. Ehlis, T. Polak, and A. J. Fallgatter, 'Altered parietal brain oxygenation in alzheimer's disease as assessed with near-infrared spectroscopy', *American Journal of Geriatric Psychiatry*, vol. 18, no. 5, pp. 433–441, 2010, doi: 10.1097/JGP.0b013e3181c65821.

[58] R. Li, G. Rui, W. Chen, S. Li, P. E. Schulz, and Y. Zhang, 'Early Detection of Alzheimer's Disease Using Non-invasive Near-Infrared Spectroscopy', *Front Aging Neurosci*, vol. 10, p. 366, 2018, doi: 10.3389/fnagi.2018.00366.

[59] C. Hock *et al.*, 'Decrease in parietal cerebral hemoglobin oxygenation during performance of a verbal fluency task in patients with Alzheimer's disease monitored by means of near-infrared spectroscopy (NIRS) - Correlation with simultaneous rCBF-PET measurements', *Brain Res*, vol. 755, no. 2, pp. 293–303, 1997, doi: 10.1016/S0006-8993(97)00122-4.

[60] I. Maidan *et al.*, 'The Role of the Frontal Lobe in Complex Walking Among Patients With Parkinson's Disease and Healthy Older Adults', *Neurorehabil Neural Repair*, vol. 30, no. 10, pp. 963–971, Nov. 2016, doi: 10.1177/1545968316650426.

[61] I. Maidan, H. Bernad-Elazari, E. Gazit, N. Giladi, J. M. Hausdorff, and A. Mirelman, 'Changes in oxygenated hemoglobin link freezing of gait to frontal activation in patients with Parkinson disease: an fNIRS study of transient motor-cognitive failures', *J Neurol*, vol. 262, no. 4, pp. 899–908, Apr. 2015, doi: 10.1007/s00415-015-7650-6.

[62] H. Obrig, 'NIRS in clinical neurology - a "promising" tool?', *Neuroimage*, vol. 85, pp. 535–546, 2014, doi: 10.1016/j.neuroimage.2013.03.045.

[63] J. Steinbrink, A. Villringer, F. Kempf, D. Haux, S. Boden, and H. Obrig, 'Illuminating the BOLD signal: combined fMRI–fNIRS studies', *Magnetic Resonance Imaging*, vol. 24, no. 4. pp. 495–505, 2006. doi: //doi.org/10.1016/j.mri.2005.12.034.

[64] M. J. Herrmann Ph.D, J. B. M. Langer M.A, C. Jacob M.D, A.-C. Ehlis M.A, and A. J. Fallgatter Prof, 'Reduced Prefrontal Oxygenation in Alzheimer Disease During Verbal Fluency Tasks', *The American journal of geriatric psychiatry*, vol. 16, no. 2, pp. 125–135, 2008, doi: 10.1097/JGP.0b013e3180cc1fbc.

[65] M. J. Herrmann, A.-C. Ehlis, and A. J. Fallgatter, 'Frontal activation during a verbal-fluency task as measured by near-infrared spectroscopy', *Brain Research Bulletin*, vol. 61, no. 1. pp. 51–56, 2003. doi: //doi.org/10.1016/S0361-9230(03)00066-2.

[66] C. Hock *et al.*, 'Near infrared spectroscopy in the diagnosis of Alzheimer's disease', *Annals of the New York Academy of Sciences*, vol. 777. 1996. doi: 10.1111/j.1749-6632.1996.tb34397.x.

[67] F. Irani, S. M. Platek, S. Bunce, A. C. Ruocco, and D. Chute, 'Functional Near Infrared Spectroscopy (fNIRS): An Emerging Neuroimaging Technology with Important Applications for the Study of Brain Disorders', *Clin Neuropsychol*, vol. 21, no. 1, pp. 9–37, Jan. 2007, doi: 10.1080/13854040600910018.

[68] K. Uludag, K. Ugurbil, and L. Berliner, Eds., *fMRI: From Nuclear Spins to Brain Functions*, vol. 30. Boston, MA: Springer US, 2015. doi: 10.1007/978-1-4899-7591-1.

[69] J. B. Mandeville and B. R. Rosen, 'Functional MRI', in *Brain Mapping: The Methods*, Elsevier, 2002, pp. 315–349. doi: 10.1016/B978-012693019-1/50015-0.

[70] T. Geva, 'Magnetic Resonance Imaging: Historical Perspective', *Journal of Cardiovascular Magnetic Resonance*, vol. 8, no. 4, pp. 573–580, Aug. 2006, doi: 10.1080/10976640600755302.

[71] P. M. Matthews and P. Jezzard, 'Functional Magnetic Resonance Imaging', in *Neuroscience for Neurologists*, PUBLISHED BY IMPERIAL COLLEGE PRESS AND DISTRIBUTED BY WORLD SCIENTIFIC PUBLISHING CO., 2006, pp. 401–422. doi: 10.1142/9781860948961_0015.

[72] J. Assländer *et al.*, 'Single shot whole brain imaging using spherical stack of spirals trajectories', *NeuroImage (Orlando, Fla.)*, vol. 73, pp. 59–70, Jun. 2013, doi: 10.1016/j.neuroimage.2013.01.065.

[73] J. Hennig *et al.*, '15 Years MR-encephalography', *Magnetic Resonance Materials in Physics, Biology and Medicine*, vol. 34, no. 1, pp. 85–108, Feb. 2021, doi: 10.1007/s10334-020-00891-z.

[74] Z. Rajna *et al.*, 'Cardiovascular brain impulses in Alzheimer's disease', *Brain*, vol. 144, no. 7, pp. 2214–2226, 2021, doi: 10.1093/brain/awab144.

[75] V. Korhonen *et al.*, 'Synchronous Multiscale Neuroimaging Environment for Critically Sampled Physiological Analysis of Brain Function: Hepta-Scan Concept', *Brain Connect*, vol. 4, no. 9, pp. 677–689, 2014, doi: 10.1089/brain.2014.0258.

[76] N. Mori, T. Suzuki, and S. Kakuno, 'Noise of Acoustic Doppler Velocimeter Data in Bubbly Flows', *J Eng Mech*, vol. 133, no. 1, pp. 122–125, Jan. 2007, doi: 10.1061/(ASCE)0733-9399(2007)133:1(122).

[77] P. van der Zee *et al.*, 'Experimentally measured optical pathlengths for the adult head, calf and forearm and the head of the newborn infant as a function of inter optode spacing', *Adv Exp Med Biol*, vol. 316, pp. 143–153, 1992, [Online]. Available: https://www.ncbi.nlm.nih.gov/pubmed/1288074

[78] L. R.Krol, 'Permutation test ', 2021. https://github.com/lrkrol/permutationTest

[79] Y. Benjamini and Y. Hochberg, 'Controlling the False Discovery Rate: A Practical and Powerful Approach to Multiple Testing', *Journal of the Royal Statistical Society. Series B, Methodological*, vol. 57, no. 1, pp. 289–300, 1995, doi: 10.1111/j.2517-6161.1995.tb02031.x.

[80] A. Wåhlin, A. Eklund, and J. Malm, '4D flow MRI hemodynamic biomarkers for cerebrovascular diseases', *J Intern Med*, vol. 291, no. 2, pp. 115–127, Feb. 2022, doi: 10.1111/joim.13392.

[81] R. N. KALARIA, 'The Blood-Brain Barrier and Cerebrovascular Pathology in Alzheimer's Disease', *Ann N Y Acad Sci*, vol. 893, no. 1 OXIDATIVE/ENE, pp. 113–125, Nov. 1999, doi: 10.1111/j.1749-6632.1999.tb07821.x.

[82] J. Ramos-Cejudo *et al.*, 'Traumatic Brain Injury and Alzheimer's Disease: The Cerebrovascular Link', *EBioMedicine*, vol. 28, pp. 21–30, Feb. 2018, doi: 10.1016/j.ebiom.2018.01.021.

[83] P. M. Pimentel-Coelho and S. Rivest, 'The early contribution of cerebrovascular factors to the pathogenesis of Alzheimer's disease', *European Journal of Neuroscience*, vol. 35, no. 12, pp. 1917–1937, Jun. 2012, doi: 10.1111/j.1460-9568.2012.08126.x.

[84] M. M. Esiri, Z. Nagy, M. Z. Smith, L. Barnetson, and A. D. Smith, 'Cerebrovascular disease and threshold for dementia in the early stages of Alzheimer's disease', *The Lancet*, vol. 354, no. 9182, pp. 919–920, Sep. 1999, doi: 10.1016/S0140-6736(99)02355-7.

[85] S. Love and J. S. Miners, 'Cerebrovascular disease in ageing and Alzheimer's disease', *Acta Neuropathol*, vol. 131, no. 5, pp. 645–658, May 2016, doi: 10.1007/s00401-015-1522-0.

[86] C. Y. Santos, P. J. Snyder, W. Wu, M. Zhang, A. Echeverria, and J. Alber, 'Pathophysiologic relationship between Alzheimer's disease, cerebrovascular disease, and cardiovascular risk: A review and synthesis', *Alzheimer's & Dementia: Diagnosis, Assessment & Disease Monitoring*, vol. 7, no. 1, pp. 69–87, Jan. 2017, doi: 10.1016/j.dadm.2017.01.005.

[87] J. A. Claassen and R. Zhang, 'Cerebral autoregulation in Alzheimer's disease', *Journal of Cerebral Blood Flow & Metabolism*, vol. 31, no. 7, pp. 1572–1577, Jul. 2011, doi: 10.1038/jcbfm.2011.69.

[88] K. Kisler, A. R. Nelson, A. Montagne, and B. v. Zlokovic, 'Cerebral blood flow regulation and neurovascular dysfunction in Alzheimer disease', *Nat Rev Neurosci*, vol. 18, no. 7, pp. 419–434, Jul. 2017, doi: 10.1038/nrn.2017.48.

[89] R. A. A. de Heus *et al.*, 'Dynamic Regulation of Cerebral Blood Flow in Patients With Alzheimer Disease', *Hypertension*, vol. 72, no. 1, pp. 139–150, Jul. 2018, doi: 10.1161/HYPERTENSIONAHA.118.10900.

[90] A. H. van Beek, J. A. Claassen, M. G. O. Rikkert, and R. W. Jansen, 'Cerebral Autoregulation: An Overview of Current Concepts and Methodology with Special Focus on the Elderly', *Journal of Cerebral Blood Flow & Metabolism*, vol. 28, no. 6, pp. 1071–1085, Jun. 2008, doi: 10.1038/jcbfm.2008.13.

[91] A. H. E. A. van Beek and J. A. H. R. Claassen, 'The cerebrovascular role of the cholinergic neural system in Alzheimer's disease', *Behavioural Brain Research*, vol. 221, no. 2. pp. 537–542, 2011. doi: 9443/10.1016/j.bbr.2009.12.047.

[92] B. Gyanwali *et al.*, 'Arterial Spin-Labeling Parameters and Their Associations with Risk Factors, Cerebral Small-Vessel Disease, and Etiologic Subtypes of Cognitive Impairment and Dementia', *American Journal of Neuroradiology*, vol. 43, no. 10, pp. 1418–1423, Oct. 2022, doi: 10.3174/ajnr.A7630.

[93] M. E. Safar, 'Systolic blood pressure, pulse pressure and arterial stiffness as cardiovascular risk factors', *Curr Opin Nephrol Hypertens*, vol. 10, no. 2, 2001, [Online]. Available: https://journals.lww.com/co-nephrolhypertens/Fulltext/2001/03000/Systolic_blood_pressure,_pulse_pressure_and.15.aspx

[94] M. Muller, Y. van der Graaf, F. L. Visseren, A. L. Vlek, W. Pt. Mali, and M. I. Geerlings, 'Blood pressure, cerebral blood flow, and brain volumes. The SMART-MR study', *J Hypertens*, vol. 28, no. 7, pp. 1498–1505, Jul. 2010, doi: 10.1097/HJH.0b013e32833951ef.

[95] A. Hatt, S. Cheng, K. Tan, R. Sinkus, and L. E. Bilston, 'MR Elastography Can Be Used to Measure Brain Stiffness Changes as a Result of Altered Cranial Venous Drainage During Jugular Compression', *American Journal of Neuroradiology*, vol. 36, no. 10, pp. 1971–1977, Oct. 2015, doi: 10.3174/ajnr.A4361.

[96] R. W. Hurst *et al.*, 'Dementia resulting from dural arteriovenous fistulas: the pathologic findings of venous hypertensive encephalopathy.', *American Journal of Neuroradiology*, vol. 19, no. 7, p. 1267, Aug. 1998, [Online]. Available: http://www.ajnr.org/content/19/7/1267.abstract

[97] C. Beggs *et al.*, 'Jugular venous reflux and brain parenchyma volumes in elderly patients with mild cognitive impairment and Alzheimer's disease', *BMC Neurol*, vol. 13, no. 1, p. 157, Dec. 2013, doi: 10.1186/1471-2377-13-157.

[98] T. NG and K. VE, 'Venous Neurovascular Pathways to Neuroinflammation in Neurodegenerative Disorders', *Interdisciplinary Journal of Microinflammation*, vol. 01, no. 01, 2014, doi: 10.4172/ijm.1000112.

[99] N. Korte, R. Nortley, and D. Attwell, 'Cerebral blood flow decrease as an early pathological mechanism in Alzheimer's disease', *Acta Neuropathol*, vol. 140, no. 6, pp. 793–810, Dec. 2020, doi: 10.1007/s00401-020-02215-w.

[100] R. B. Nielsen *et al.*, 'Capillary dysfunction is associated with symptom severity and neurodegeneration in Alzheimer's disease', *Alzheimer's & Dementia*, vol. 13, no. 10, pp. 1143–1153, Oct. 2017, doi: 10.1016/j.jalz.2017.02.007.

[101] L. A. Rivera-Rivera *et al.*, 'Changes in intracranial venous blood flow and pulsatility in Alzheimer's disease: A 4D flow MRI study', *Journal of Cerebral Blood Flow & Metabolism*, vol. 37, no. 6, pp. 2149–2158, Jun. 2017, doi: 10.1177/0271678X16661340.

[102] I. Silva, J. Silva, R. Ferreira, and D. Trigo, 'Glymphatic system, AQP4, and their implications in Alzheimer's disease', *Neurol Res Pract*, vol. 3, no. 1, p. 5, Dec. 2021, doi: 10.1186/s42466-021-00102-7.

[103] V. Mondejar and A. Patsalides, 'The Role of Arachnoid Granulations and the Glymphatic System in the Pathophysiology of Idiopathic Intracranial Hypertension', *Curr Neurol Neurosci Rep*, vol. 20, no. 7, p. 20, Jul. 2020, doi: 10.1007/s11910-020-01044-4.